Institutionen för medicin och vård
Avdelningen för radiofysik
Hälsouniversitetet

Implementation of unsharpness and noise into the model of the imaging system: Applications to chest and lumbar spine screen-film radiography

Michael Sandborg, David R Dance and
Gudrun Alm Carlsson

Department of Medicine and Care
Radio Physics
Faculty of Health Sciences

Series: Report / Institutionen för radiologi, Universitetet i Linköping; 90
ISRN: LIU-RAD-R-090

Publishing year: 1999

Report 90
Jan. 1999 ISRN ULI-RAD-R--90--SE

Implementation of unsharpness and noise into the model of the imaging system: Applications to chest and lumbar spine screen-film radiography

M Sandborg[1], D R Dance[2], and G Alm Carlsson[1]

1. Department of Radiation Physics, IMV, Linköping University
2. Joint Department of Physics, The Royal Marsden NHS Trust

Full addresses:

1. Department of Radiation Physics, IMV,
Faculty of Health Sciences,
Linköping University,
SE-581 85 LINKÖPING, Sweden
Fax ++46 13 224749
E-mail: Michael.Sandborg@raf.liu.se
Gudrun.Alm.Carlsson@raf.liu.se

2. Joint Department of Physics,
The Royal Marsden NHS Trust and
Institute of Cancer Research,
Fulham Road,
London SW3 6JJ,
United Kingdom
Fax ++44 171 349 0059
E-mail: d.dance@icr.ac.uk

Table of Contents

Introduction

A model of the complete x-ray imaging system including the patient is a powerful tool for imaging system analysis and the optimisation of image quality and patient dose. It allows flexible variation of the system components (i.e. x-ray source, anti-scatter device and image detector) and study of their effect on image quality and patient risk. Our group has developed, validated and calibrated (McVey et al. 1997, 1998) a Monte Carlo model of the complete imaging system for chest and lumbar spine examination including voxalised human male anatomy (Zubal 1994). The Monte Carlo program calculates the contrast and signal-to-noise ratio (SNR) of various contrasting details within the voxel phantom. Important details in the images have been selected by consulting radiologist (Hammerby, Wirell and ???) and the EU document of image quality criteria (Carmichael et al 1996). The entrance surface dose without back-scatter and the effective dose are used as measures of patient radiation risk.

The contrasts of the details are derived initially from Monte Carlo estimates of the energy imparted per unit area to the image detector beside and behind the detail. However, this ignores the effects of unsharpness in the imaging chain (such as screen-film, geometric and motion unsharpness) and the influence on contrast of the film characteristic curve. In the Monte Carlo program, SNR is calculated assuming that the noise arises from the random fluctuations in the energy imparted per unit area to the image detector only. However, other noise sources also contribute to the total noise, such as screen and film noise. Hence the model of the imaging system needs to be further developed to take these effects into account. The methods used to extend the model are described below together with illustrations of their effect on the difference in optical density, ΔOD, and SNR in chest and lumbar spine imaging.

Objective

The objective for the present report is to describe how the x-ray imaging system unsharpness and additional detector noise can be implemented to complement a Monte Carlo model of the x-ray imaging system that includes the random fluctuations in the energy imparted to the detector (quantum noise). The Monte Carlo program simulates the x-ray examination and calculates the contrast and signal-to-noise ratio (SNR) of various important details within the human normal anatomy represented by a 3D voxel phantom (Zubal 1994). Values of the image quality descriptors (contrast and SNR) are derived from calculations of the expectation value and variance of the energy imparted per unit area to the image detector beside and behind the detail. However, the effects on the image quality of unsharpness in the imaging chain, additional detector noise and the film characteristic curve are not included in the Monte Carlo model but have to be included in a post-processing procedure. Methods to explore these effects on contrast and SNR are developed and described in this report. The methods used are to a large extent taken from the literature and have been implemented using MATLAB® software (The Math Works Inc. 1997).

Strategy

The strategy is, for each size and shape of the contrasting detail, to calculate correction factors to the Monte Carlo derived values of contrast and SNR. The loss in contrast due to unsharpness is expressed by the reduction in the maximum (peak) amplitude of the signal in the shadow area of the detail compared to the signal amplitude without any influence of unsharpness. It is derived by calculating the inverse Fourier transform of the product of the system modulation transfer function and the spatial-frequency content of the attenuation profile of the detail. The influence of film contrast is included by means of the film characteristic (H&D) curve. The concept of the ideal observer is used for calculating the SNR. The Monte Carlo derived SNR assumes that the only source of noise is that due to the fluctuations in the energy imparted to the detector. This underestimates the noise particularly in regions with low and high optical densities due to significant film noise. The additional noise sources are included by applying three correction factors to the SNR^2 derived using the model of Nishikawa and Yaffe (1990). The correction factors take values between zero and unity. The first factor expresses the quotient of the quantum noise to the total (screen plus film) noise, the second factor the loss in SNR due to the lower transfer efficiency of the signal compared to the noise through the screen. This is due to the screen's finite thickness and the different point spread functions for the light photons emitted at different depths in the screen. The third correction factor is the statistical factor, I_L, which is separately included. This factor allows for additional fluctuations in the number of the light photons reaching the film emulsions.

Application

The methods are applied and the effects of unsharpness and added noise on ΔOD and SNR for the detection of small, low-contrast details are given in chest PA and lumbar spine AP.

2. Unsharpness

Three sources of unsharpness are considered. These are screen-film system (detector) unsharpness, geometric (focal spot size and magnification) unsharpness and motion (patient movement) unsharpness. The relative importance of each will vary with the application. The implementation of each of the unsharpness sources is described below and examples of their application to chest and lumbar spine imaging are given.

2.1. Screen-film system unsharpness

By far the largest contribution to screen-film unsharpness is due to the lateral spread of the light photons as they travel from the screen phosphor to the film emulsion. The amount of spread depends on the thickness of the phosphor, the depth distribution of the energy imparted to the screen, the presence of dye and reflective backing in the screen, and the thickness of the screen's protective coating. It is common to use two screens surrounding a double emulsion film. The crossover of light through the film base will then also influence the unsharpness. The spatial distribution of the energy imparted by the x-ray photons to the two screens depends primarily on the attenuation of these photons in the screens and the diffusion and absorption of the secondary K-photons from the high-Z elements in the screen phosphor material. It depends to some extent also on the range of the liberated secondary electrons.

2.1.1. Implementation

Screen-film unsharpness is generally quantified by the modulation transfer function (MTF) of the screen-film system, MTF_{scr}. This was measured (Verdun et al 1997 and 1998, personal communication) either by exposing a 10 μm wide slit in contact with the screen-film system (obtaining the line spread function, LSF) or by the grating method (DIN 1985).

Data on MTF_{scr} are available from the literature but often only for a limited number of x-ray spectra. A small dependence of the MTF on the x-ray photon energy can be expected (Karlsson 1983) since the generation of K fluorescent photons in the phosphor material is strongly energy dependent. Also the depth distribution of the energy imparted to the screen depends on photon energy. This may cause a change in MTF due to the different transfer efficiency of the light to the film from different depths in the screen. A model that incorporates the energy-dependence of the detector unsharpness was developed by Sandborg *et al.* (1996). To use this model was, however, unnecessarily complicated for the purpose of this work and, therefore, the screen-film unsharpness was quantified by the measured MTF_{scr} determined at one single tube potential relevant for the two x-ray examinations; chest or lumbar spine.

2.1.2. Application

Measured modulation transfer functions, MTF_{scr} for the four screen-film systems used by all partners in the project and employed in the clinical trials are shown in figure 1. The Kodak Lanex 160 and Lanex 320 screens with Kodak TML film are used in the chest examinations, and the Kodak Lanex Regular and Lanex Fast with

Kodak TML film are used in the lumbar spine examination. The additional two screen-film systems (figure 2) for chest (Agfa Curix Ortho Medium/ Fuji HRL) and lumbar spine (Kodak Lanex Medium/ Fuji HRE) imaging were used in Linköping for calibration and validation of the Monte Carlo model.

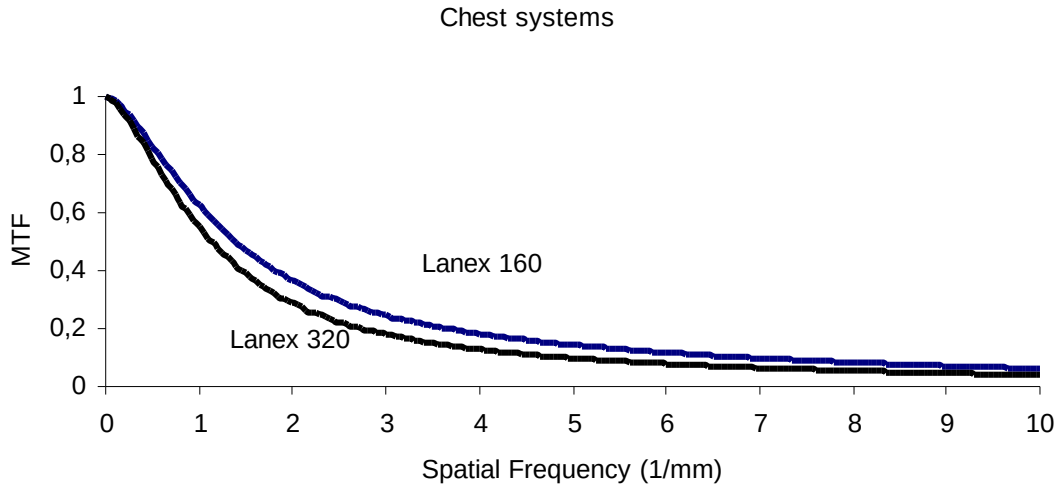

Figure 1a. The measured modulation transfer function, MTF_{scr} for a Kodak Lanex 160 and a Lanex 320 screen-film system (Verdun et al, personal communication, 1998).

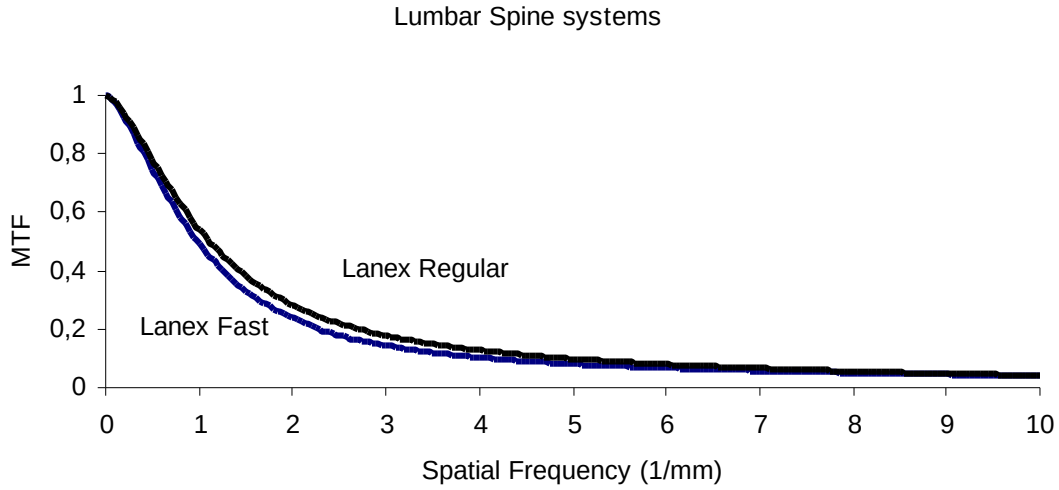

Figure 1b. The measured modulation transfer function, MTF_{scr} for a Kodak Lanex Regular and a Lanex Fast screen-film system (Verdun et al, personal communication, 1998).

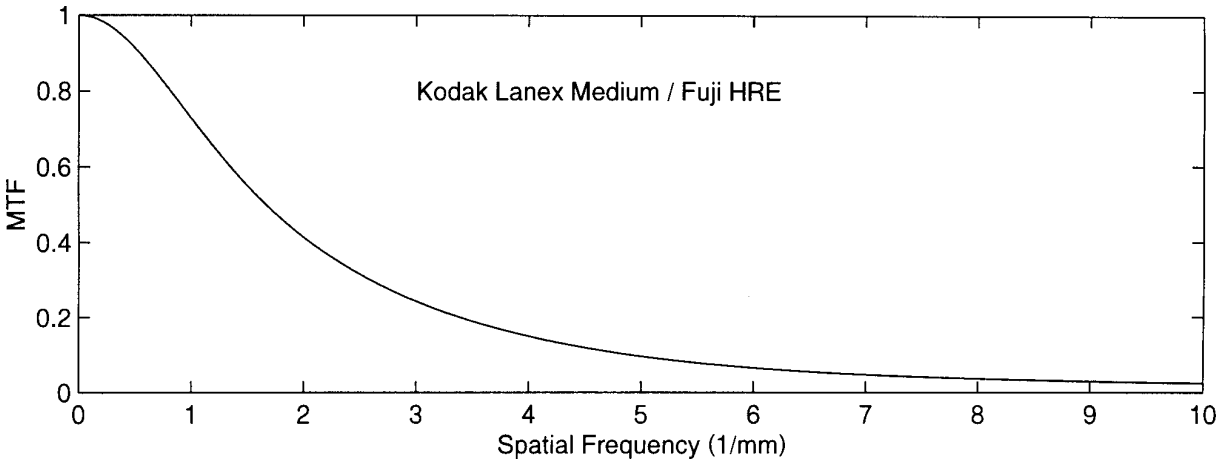

Figure 2a. The measured modulation transfer function, MTF_{scr} for a Kodak Lanex Medium/Fuji HRE screen-film system (Verdun et al, personal communication, 1997).

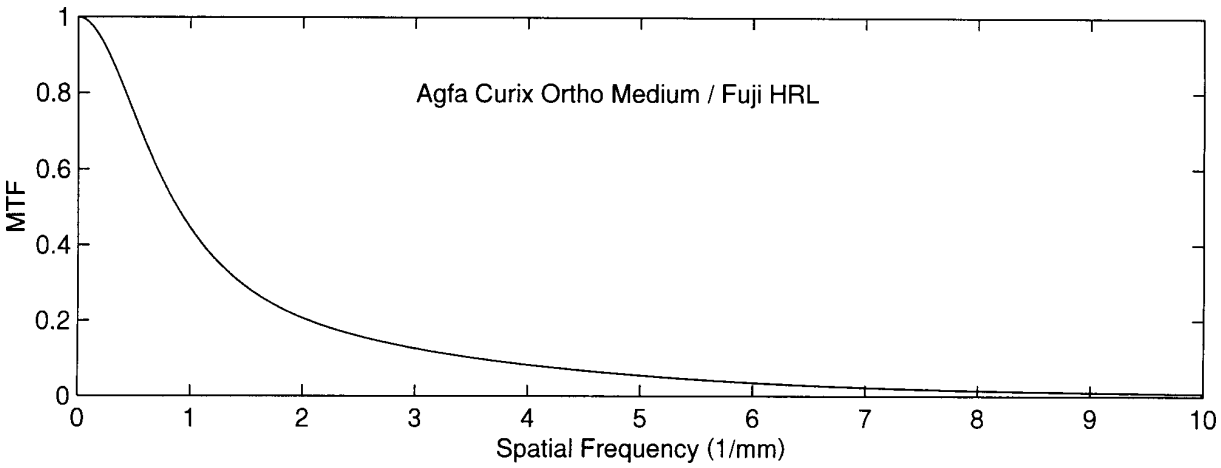

Figure 2b. The measured modulation transfer function, MTF_{scr} for an Agfa Curix Ortho Medium/Fuji HRL screen-film system (Verdun et al, personal communication, 1997).

2.2. Geometric unsharpness

The geometric unsharpness is caused by the finite size of the focal spot and varies with the magnification. The increase in size of any detail within the patient is due to the divergent beam and the distance between the detail and the image plane and the focus-film distance. The focal spot can be well characterised using a direct measurement with a pinhole camera, or with any equipment that enables recording of a magnified image of the emission distribution from the focal spot.

2.2.1. Implementation

The magnification depends on the focus-film distance, FFD, and the distance between the focal spot and the detail to be imaged, focus-detail distance, FDD. For

thin details, the distance between the detail and the film, the detail-film distance, DFD is therefore FFD-FDD. The magnification m is given by

$$m = FFD/FDD = 1 + DFD/FDD. \quad (1)$$

The focal spot is asymmetric and will have different lengths parallel and perpendicular to the anode-cathode axis. Its projected area (size) varies with position in the image. This complication is not modelled here but is allowed for to some extent in studying the effects of varying the focal spot size.

The size of the focal spot also varies with the applied tube potential (U) and tube current (I). Chaney and Hendee (1974) found that the size of the focal spot could be modelled by assuming that it is proportional to the tube current (I) and inversely proportional to $U^{3/2}$.

The focal spot intensity distribution can be modelled in various ways. Probably the simplest is the 'box'function, i.e., uniform emission distribution within a box of side f_0 and no emission outside the box. The area of the focus is then f_0^2 and the MTF for geometric unsharpness, MTF_{geo} (Rao et al. 1973 and Lubberts and Rossmann 1967) given by

$$MTF_{geo} = \left|\sin(pf_0n(m-1))/pf_0n(m-1)\right| \quad (2)$$

where ν is the spatial frequency in the image plane and (m-1)=DFD/FDD. Both the spatial frequency ν in the image plane and the spatial frequency in the object plane ν_0 are of interest. The relation between the two is

$$\nu = \nu_0/m. \quad (3)$$

Other focal spot shapes that can be included are: circular (Sandrik and Wagner 1982), triangular (Rao *et al.* 1973) and Gaussian shaped (Prasad *et al.* 1976). Using the Gaussian shaped focal spot emission profile, the size can be characterised by the standard deviation of the distribution, σ, and the MTF_{geo} is then given by (Prasad *et al.* 1976)

$$MTF_{geo} = \exp(-2p^2 \cdot s^2 \cdot \nu^2 \cdot (m-1)^2) \quad (4)$$

It is assumed here that the full width at half maximum (FWHM) of the Gaussian distribution characterises the width, f_0, of the distribution. The FWHM and the standard deviation, σ, are related by FWHM=2.35 σ.

2.2.2. Application

The values of the nominal focal spot size, f_0 to be modelled should vary between 0.3-2.0 mm. It is anticipated that the magnifications encountered in a lumbar spine examination would be between 5-40%. In the chest examination the FFD is usually

larger than in a lumbar spine examination if an air gap (increased DFD) is used, resulting in magnifications in the same range as for lumbar spine.

In figure 3, the geometric unsharpness, MTF_{geo} is shown for three different focal spot sizes (f_0=0.6, 1.2 and 2.0 mm box-shaped) at m=1.05. The MTF_{geo} is significantly reduced as the focal spot size increases. The MTF_{geo} is, however, still large compared to the MTF_{scr} (figs. 1 and 2) at this comparably small magnification.

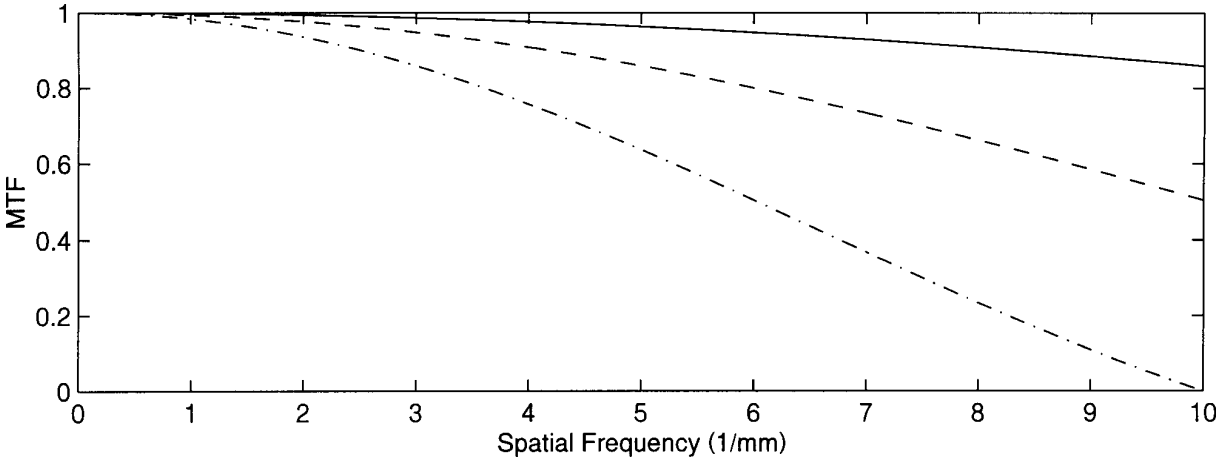

Figure 3. The MTF of geometrical unsharpness, MTF_{geo} as function of spatial frequency in the image plane for three different focal spot sizes (f_0=0.6 mm (——), 1.2 mm (- - -) and 2.0 mm (- . - . -)) at m=1.05 and using a box-shaped emission profile.

In figure 4, MTF_{geo} is shown for different magnifications (m=1.05, 1.15 and 1.25) at f_0=0.6 mm. The MTF_{geo} rapidly decreases with increasing magnification and is at m=1.25 the limiting unsharpness component in the imaging system at the higher spatial frequencies ν>6.5 mm^{-1}.

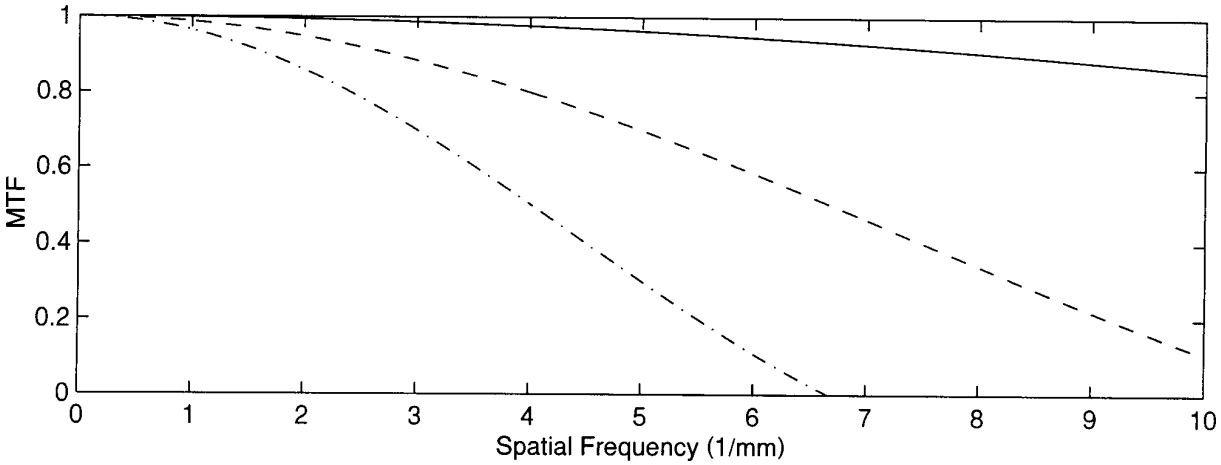

Figure 4. The MTF of geometrical unsharpness, MTF_{geo} as function of spatial frequency in the image plane for three different magnifications (m=1.05 (——), 1.15 (- - -) and 1.25 (- . - . -)) at f_0=0.6 mm (box-shaped emission profile). The MTF has been truncated at the first zero crossing.

In figure 5, the influence on MTF of the shape of the focal spot is shown (f_0=1.2 mm and m=1.05). The Gaussian-shaped focal spot yields significantly lower MTF_{geo} due to the tails of the Gaussian distribution.

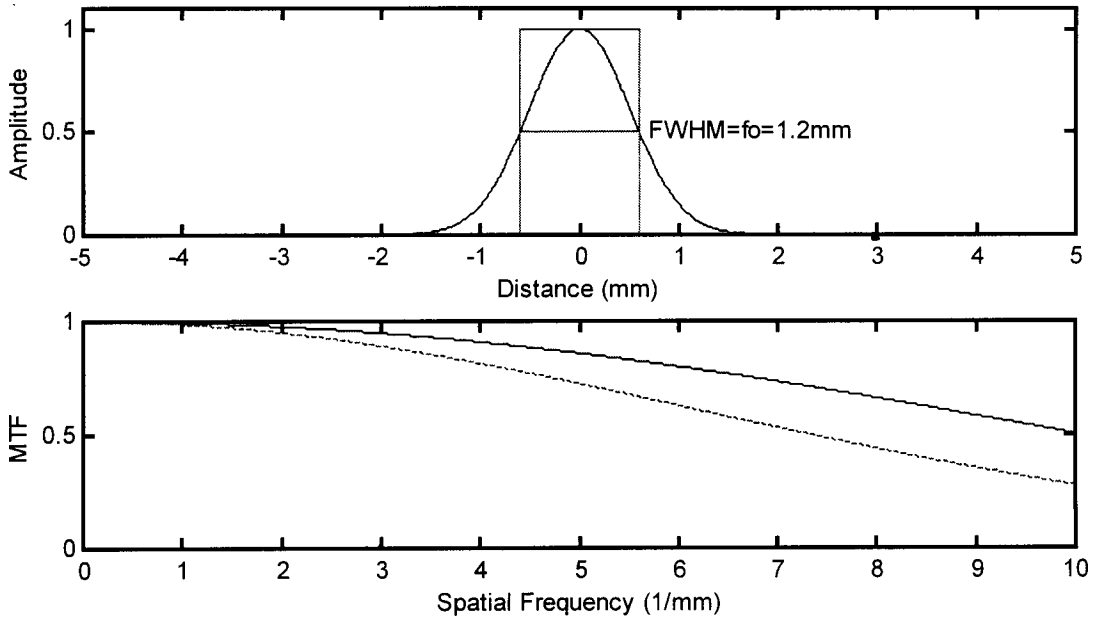

Figure 5. (a) The line profile through the centre of the emission distribution of a box-shaped and a Gaussian-shaped focal spot. The FWHM (=2.35·σ; σ=standard deviation) of the Gaussian profile is equal to the side in the box, i.e. the focal spot size is f_0=1.2 mm in both in cases. (b) The geometrical unsharpness, MTF_{geo} in the image plane for the two emission profiles: box-shaped (upper curve), and Gaussian-shaped (lower curve) at m=1.05.

Figure 6 shows the effect on MTF_{geo} as the size of the focal spot changes due to variations in tube potential and tube current. The tube potential and tube current were varied such that the output from the x-ray tube remained the same and proportional to $U^2 \cdot I$. Typically, a high tube potential and a low tube current yield the highest MTF_{geo}.

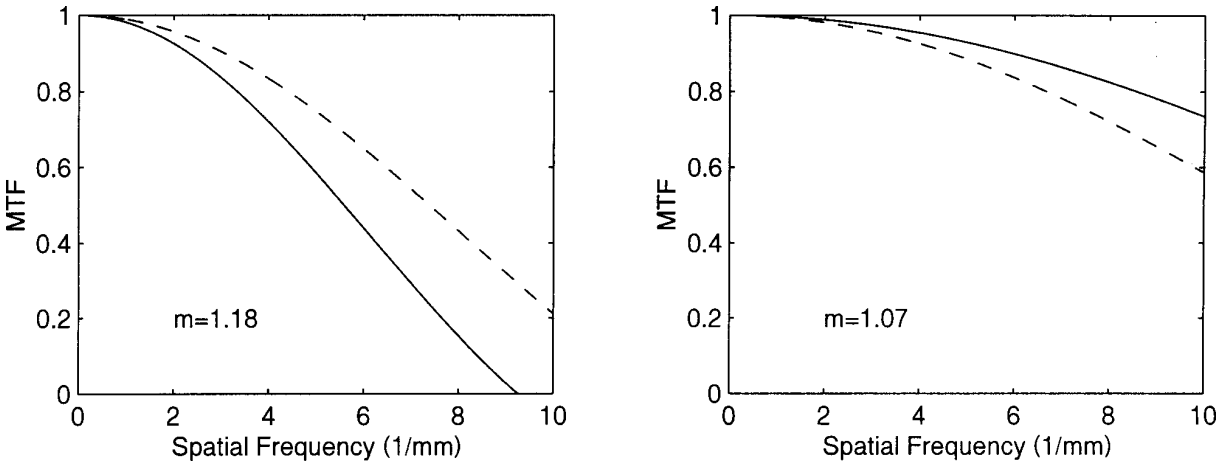

Figure 6. Illustration of the effect on MTF_{geo} of so called focal spot blooming for a box-shaped focal spot. The geometrical unsharpness, MTF_{geo} in the image plane is shown for two different combinations of tube potential and tube current, resulting in approximately the same x-ray output fluence. The magnification, m, is shown in the figures. Ledgends:
Left: 70 kV, 500 mA (f_0=0.6 mm (———), 90 kV, 300 mA (f_0=0.45 mm (- - -).
Right: 140 kV, 320 mA (f_0=0.6 mm (———), 100 kV, 630 mA (f_0=0.78 mm (- - -).

In figure 7a, the model of Chaney and Hendee (1974) has also been used to calculate the variations of the size of the focal spot at different tube potential for approximately constant output fluence. The size at 70 kV is chosen to be 0.6 mm. Figure 7b shows the MTF_{geo} at 3 mm^{-1} as function of the tube potential and demonstrates the rapid decrease in MTF_{geo} (m=1.18) at tube potentials <60 kV. Figure 7c, shows the MTF_{geo} for three tube potentials. At tube potentials >70 kV, the total system unsharpness will in most cases be dominated by the screen-film unsharpness. However, at 50 kV, the larger focal spot size will influence the total system MTF. The empirical results of Chaney and Hendee (1974) should be used carefully since it is likely that the technical solution and the dependence on tube potential and current will be different for different x-ray tube manufacturers. In addition, the design of x-ray tubes have improved significantly since 1974.

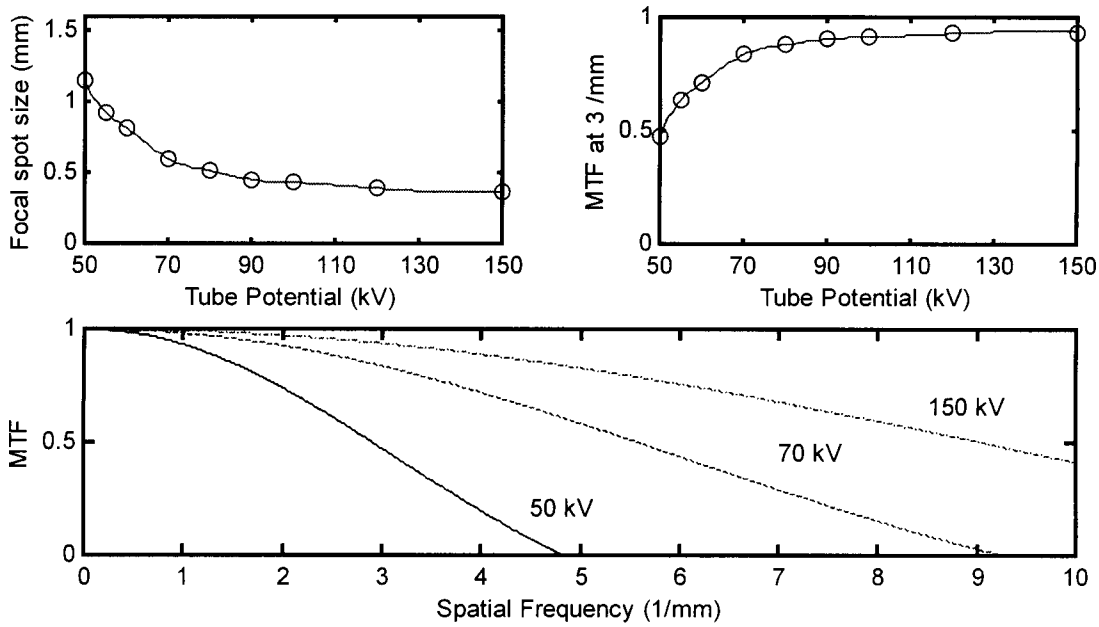

Figure 7. (a) The size of the focal spot (box-shaped) as a function of the tube potential at (approximately) constant x-ray output. Hence, the tube current varies being 980 mA at 50 kV and 110 mA at 150 kV. The focal spot size at 70 kV and 500 mA is 0.6 mm (m=1.18). (b) The MTF_{geo} at a spatial frequency of 3 mm^{-1} as a function of the tube potential for the focal spot sizes in (a). (c) The corresponding MTF_{geo} at 50 kV (f_0=1.15 mm), 70 kV (f_0=0.60mm), and 150 kV (f_0=0.37mm).

2.3. Motion unsharpness

In principle, the movements of the source, the patient and the detector will all contribute to the total motion unsharpness. In practice, however, motion unsharpness is due to the patient movement only.

2.3.1. Implementation

Morgan (1962) showed that the MTF due to patient motion, MTF_{mot} is given by

$$MTF_{mot} = \left|\sin(p \cdot h \cdot n \cdot t \cdot m)/(p \cdot h \cdot n \cdot t \cdot m)\right| \qquad (5)$$

where h is the speed at which the imaged structure moves in a direction parallel to the image plane and t is the exposure time. If the movement is not parallel to the image plane, the actual speed should be reduced by a factor cosθ, where θ is the angle between the image plane and the direction of motion. If all directions of motion are equally probable, the average resultant in the image plane is given by

$$\int_{q=0}^{q=p/2} \cos(q) \cdot \frac{2p\sin(q)}{2p} dq = 0.50 \qquad (6)$$

since the probability of an angle θ between θ, θ+dθ is $\frac{2p\sin(q)}{2p}dq$.

2.3.2. Application

Vañò (personal communication, 1997) has estimated the minimum and maximum speed of different organs of interest in a chest examination, for example the heart and lung vessels. According to this reference, the speed of motion ranges between 5.7-200 mm/s (heart) and 0.2-133 mm/s (lung vessels). Motion unsharpness is not assumed important in lumbar spine imaging in spite of the longer exposure times used.

Figure 8 shows the strong influence of motion speed and exposure time on MTF_{mot}. Especially in chest imaging it is important to keep exposure times short as some important details within the lung-heart region may move at a significant speed. Even at an exposure time of only 3 ms (used in the chest PA), a motion speed of 100 mm/s causes motion unsharpness to be the limiting factor at spatial frequencies above 5 mm^{-1}. In the lateral view, where the exposure time is typically four times longer, a motion speed of 25 mm/s will have the same effect on unsharpness. If the tube current could be increased further, exposure time and motion unsharpness could be reduced.

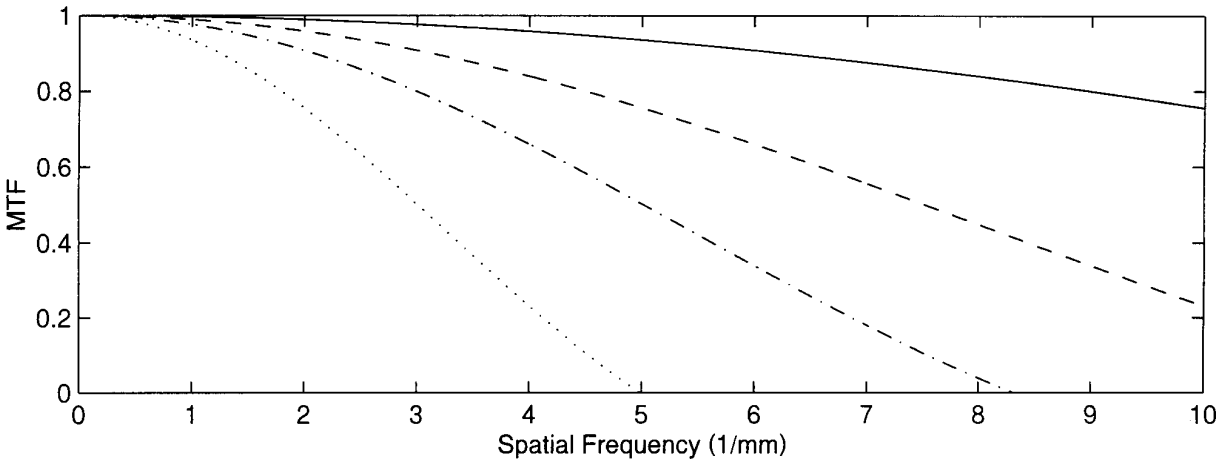

Figure 8. The MTF of motion unsharpness, MTF_{mot} as function of the spatial frequency in the image plane for four combinations of motion speed and exposure time. 20 mm/s and 3 ms (———), 20 mm/s and 6 ms (- - -), 20 mm/s and 9 ms (- . - . -), and 100 mm/s and 3 ms (·····). Magnification is m=1.05. The MTF_{mot} has been truncated at the first zero crossing.

2.4. Combined effect of motion and screen-film unsharpness

If long exposure times are a problem, one may want to consider increasing the sensitivity (speed) of the screen-film system, in spite of the concomitant decrease in MTF_{scr} typically found for such systems. The total MTF of the imaging system can be computed as the product of the individual MTF components such that:

$$MTF_{tot} = MTF_{scr} \cdot MTF_{geo} \cdot MTF_{mot} \qquad (7)$$

Motion unsharpness depends strongly on the exposure time and thus indirectly on the sensitivity of the screen-film system. In figure 9, a comparison is made of two different screen-film systems (Kodak Lanex screen) with different MTF and sensitivity at varying degrees of motion unsharpness. The Lanex Fine screen is less sensitive than the Lanex Medium screen, and requires an exposure, which is 2.62 times longer (Doi *et al*. 1986) to obtain the same optical density on the film. At zero motion speed, the exposure time is not important and the system's total MTF_{tot} depends primarily on MTF_{scr} (fig 9a); the MTF for the Lanex Fine system being significantly larger. (It is assumed here for simplicity that the geometric unsharpness is insignificant compared to the other sources of unsharpness). In fig 9b, a motion speed of 30 mm/s reduces the total MTF_{tot}, particularly for the Lanex Fine system where the exposure time is 7.9 instead of 3.0 ms. At a motion speed of 60 mm/s, the MTF_{tot} of the two systems are almost identical up to ν=2 mm^{-1} and at 120 mm/s the Lanex Medium system shows the highest MTF_{tot}. This means that when motion unsharpness is a problem, changing to a more sensitive detector may both increase sharpness and reduce patient dose.

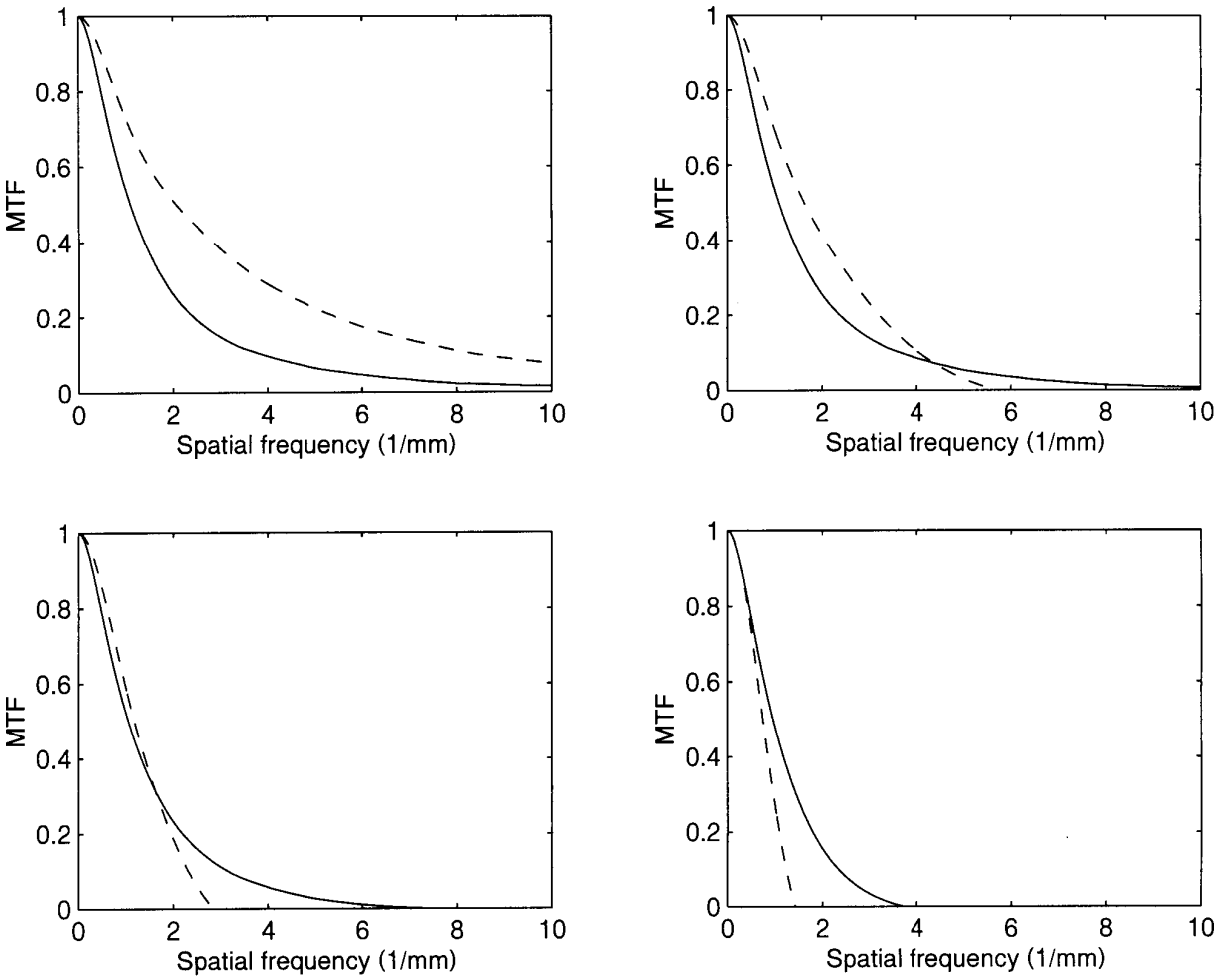

Figure 9. The combined effect of motion and screen unsharpness MTF, ($MTF_{scr} \cdot MTF_{mot}$) as function of the spatial frequency in the image plane at different degrees of motion unsharpness (increasing from a to d). Lanex Medium system (——) and Lanex Fine system (- - -). Motion speeds are 0 mm/s, 30 mm/s, 60 mm/s, and 120 mm/s in a, b, c, and d, respectively. The exposure times were 3.0 ms and 7.9 ms (3.0 ms · 2.62) using the Medium and Fine screens, respectively. Magnification is 1.17.

3. Influence of system MTF on the contrast of details

The MTF of the system gives information on how well different frequencies are transferred from the input (x-ray beam) to the output (x-ray film). As details within the body are of different size they contain different amplitudes of these frequencies. Small details contain a larger fraction of higher spatial frequencies than larger details and it is therefore important to consider the spatial-frequency content of the detail to be imaged.

3.1. Contrasting detail spatial frequency spectrum

The spatial-frequency content of the contrasting detail, $\Delta S(\nu)$ depends on its size and shape. For a detail with a Gaussian transmission profile, the size can defined by the

full width at half maximum (FWHM). The frequency content is given (Jennings et al. 1993) by

$$\Delta S(n) = 2ps^2m^2 \cdot \exp(-2p^2s^2m^2n^2) \qquad (8)$$

where σ is the standard deviation of the Gaussian distribution, σ=FWHM/2.35.

For a disk-shaped ('top-hat') detail with diameter d, the frequency content is given by

$$\Delta S(n) = m \cdot d \cdot J_1(2p \cdot n \cdot d \cdot m/n) \qquad (9)$$

where J_1 is a Bessel function of the first order.

Other shapes can also be considered such as: nodules and vessels (Ziskin *et al.* 1971).

Details of different widths are considered ranging from 0.3 and 10 mm in the Monte Carlo model (see for example Sandborg *et al.* 1997). Figures 10 and 11 show the frequency content of disk and Gaussian shaped details, respectively of width 0.5 mm and 2 mm. Due to the magnification used (m=1.2) the actual widths of the details in the image plane are 0.6 and 2.4 mm, respectively.

(a)

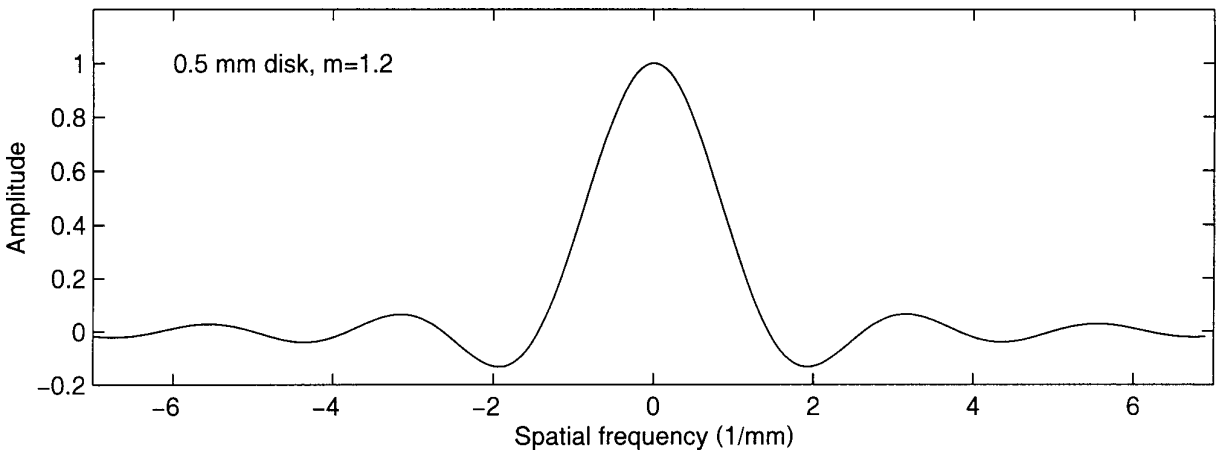

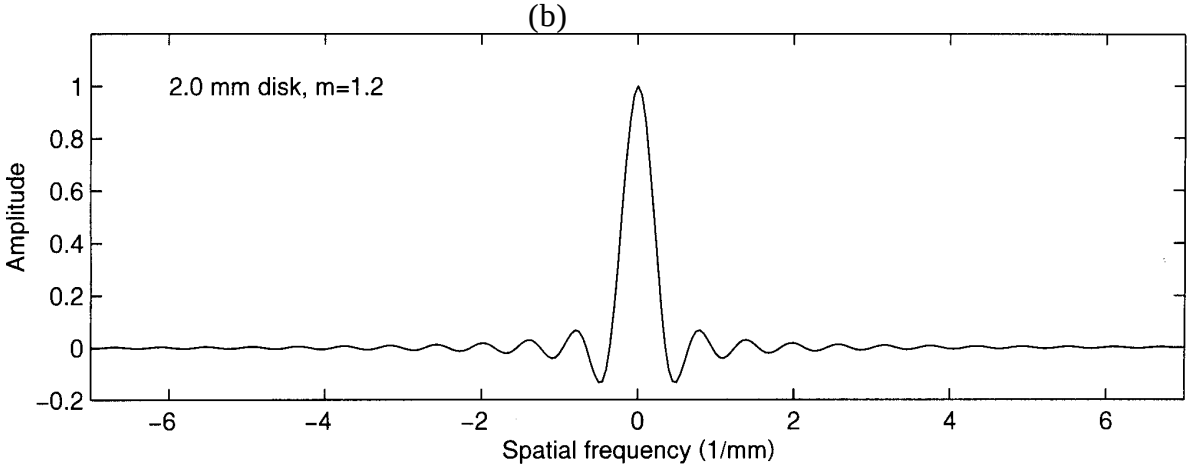

Figure 10. Spatial frequency content of details with a disc-shaped transmission profile and with diameters of 0.5 mm (a), and 2.0 mm (b). Magnification 1.2.

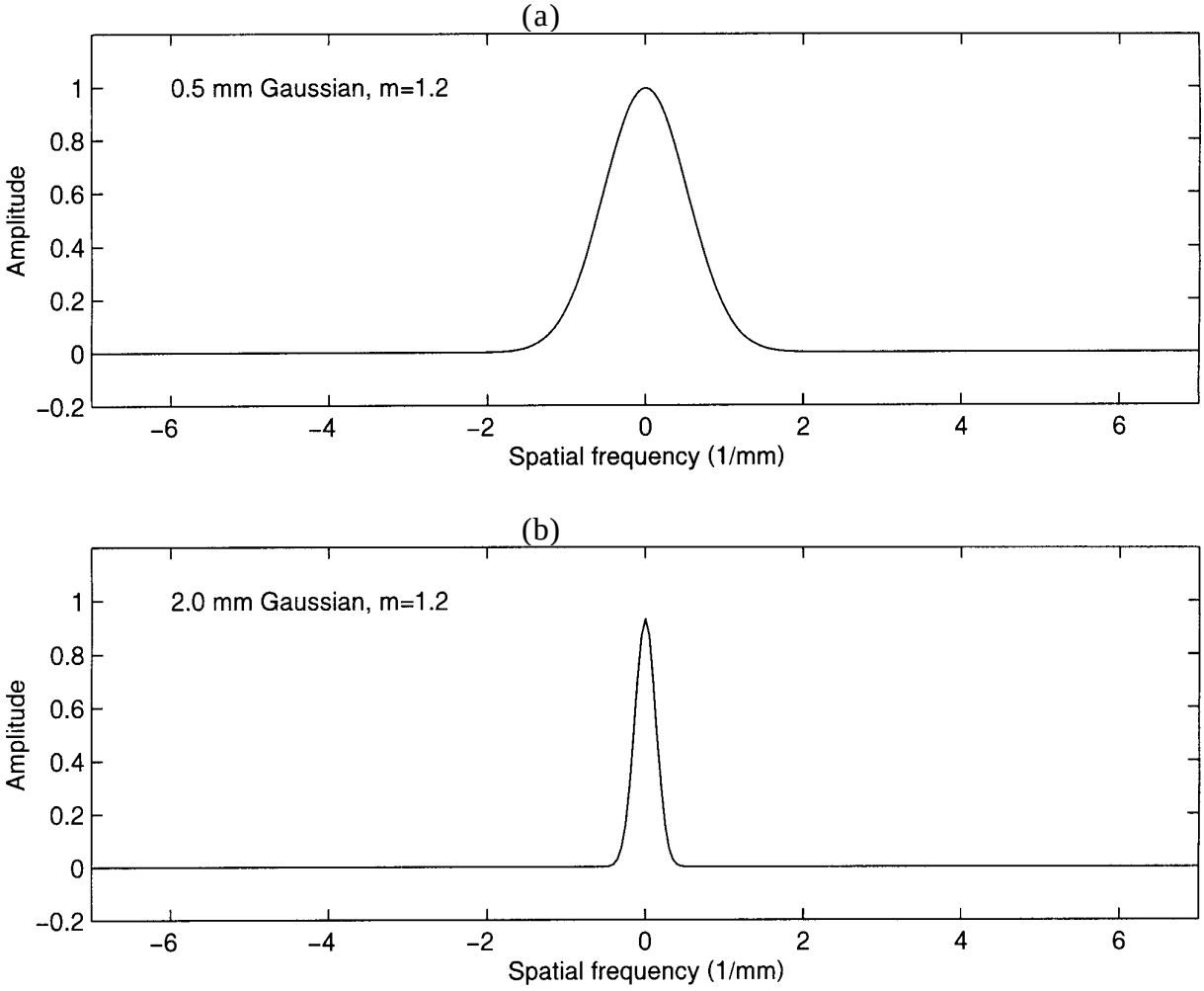

Figure 11. Spatial frequency content of details with a Gaussian transmission profile and with σ =0.5 mm (a), and σ =2.0 mm (b). Magnification 1.2.

3.2. Influence on the contrast of the detail

In order to study the effect of total MTF_{tot} on the contrast of the imaged detail, Δs, the frequency content of the detail, ΔS, in the image plane is multiplied by the MTF_{tot}. The MTF_{tot}-modified frequency content ΔS_{mod} is subsequently Fourier transformed (FT), and the modified detail, Δs_{mod}, displayed.

$$\Delta S_{\mathrm{mod}}(n) = \Delta S(n) \cdot MTF_{tot}(n)$$
$$\Delta s_{\mathrm{mod}} = FT^{-1}[\Delta S_{\mathrm{mod}}(n)] \qquad (10)$$

The images of the original (unmodified) attenuation profile of the detail, Δs, and of the modified, Δs_{mod}, profile are shown in figures 12 and 13 for disc and Gaussian shaped details of 0.5 mm.

One way to quantify the effect on contrast of the unsharpness is to use line profiles through the centre of the images of the original (unmodified) detail, Δs, and of the modified detail, Δs_{mod}. The reduction in contrast can then be defined by the ratio of the peak amplitude (P) in the original to that in the modified (P_{mod}) image (see middle figure in figs. 12-13). The contrast degradation factor due to the imaging system MTF, cdf_{MTF} is thus here defined as

$$cdf_{MTF} = \frac{P_{\mathrm{mod}}}{P} \qquad (11)$$

The contrast of the detail or the difference in optical density in the image can be computed as

$$\Delta OD = \log_{10}(e) \cdot g(OD_{\mathrm{det}}) \cdot C_e \cdot cdf_{MTF} \qquad (12)$$

where C_ε is the contrast in terms of energy imparted (ε) to the screen from primary and scattered (s) photons beside (p2) and behind (p1) the detail. C_ε is obtained from the Monte Carlo simulation. The film gradient, $\gamma(OD_{det})$ at the optical density, OD_{det}, in the background is taken from the first derivative of the film characteristic curve (Herrmann 1998, personal communication). The degradation factor cdf_{MTF} is defined above. The contrast in terms of energy imparted to the screen from primary and scattered photons from the Monte Carlo calculation is given by (Dance *et al*. 1992)

$$C_e = \frac{E(e_{p1}) - E(e_{p2})}{E(e_{p1})} \cdot \frac{1}{1 + E(e_s)/E(e_{p1})} \qquad (13)$$

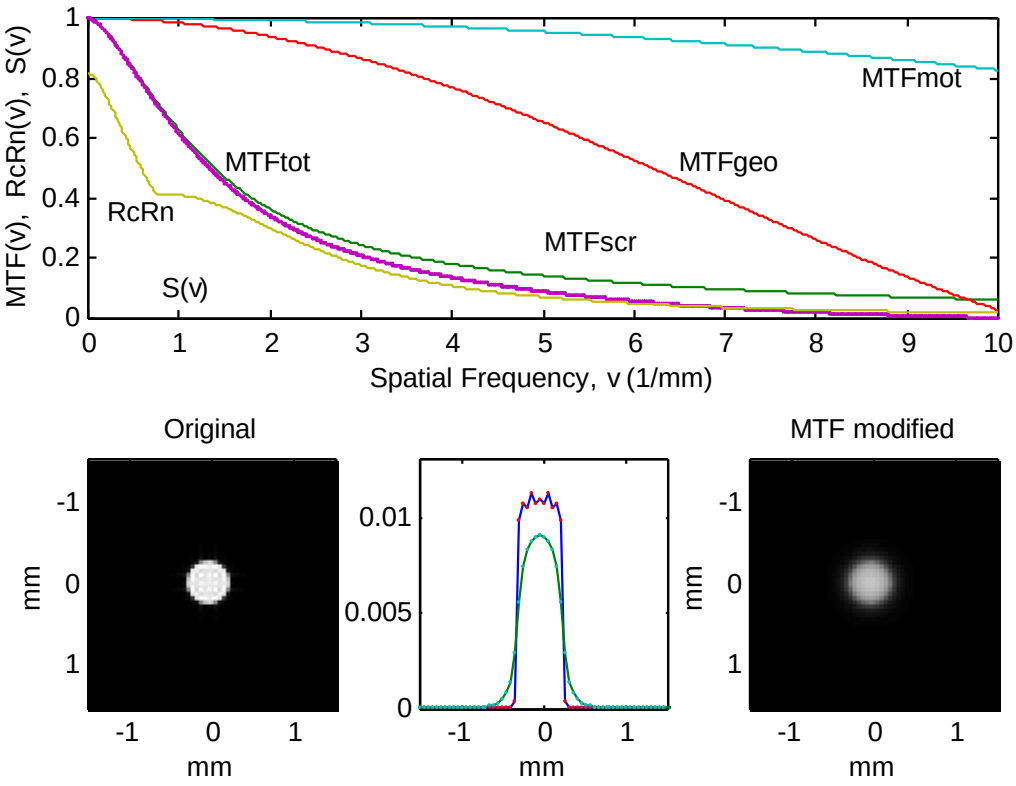

Figure 12 The components of the MTF of the chest system: the spatial-frequency content of a disc-shaped 0.5 mm detail (ΔS(ν)), and the RcRn-noise-factor (see section 4.2 for explanation). MTF_{mot} and MTF_{geo} are marked in the figure. MTF_{scr}: (- - -), MTF_{tot}: lower bold solid line (——), RcRn-factor: (- · -) and ΔS(ν): (... ... ..). The image to the left shows the original (unmodified) image of a disc-shaped detail with 0.5 mm diameter (m=1.11) and the image to the right the MTF-modified image. The figure in the middle shows the profiles through each centre. In this case the reduction in peak contrast is cdf_{MTF} = 0.837. A Kodak Lanex 160 screen, a 'box'-shaped focal spot (f_0=0.9 mm), 20 mm/s motion speed and 3 ms exposure time were used.

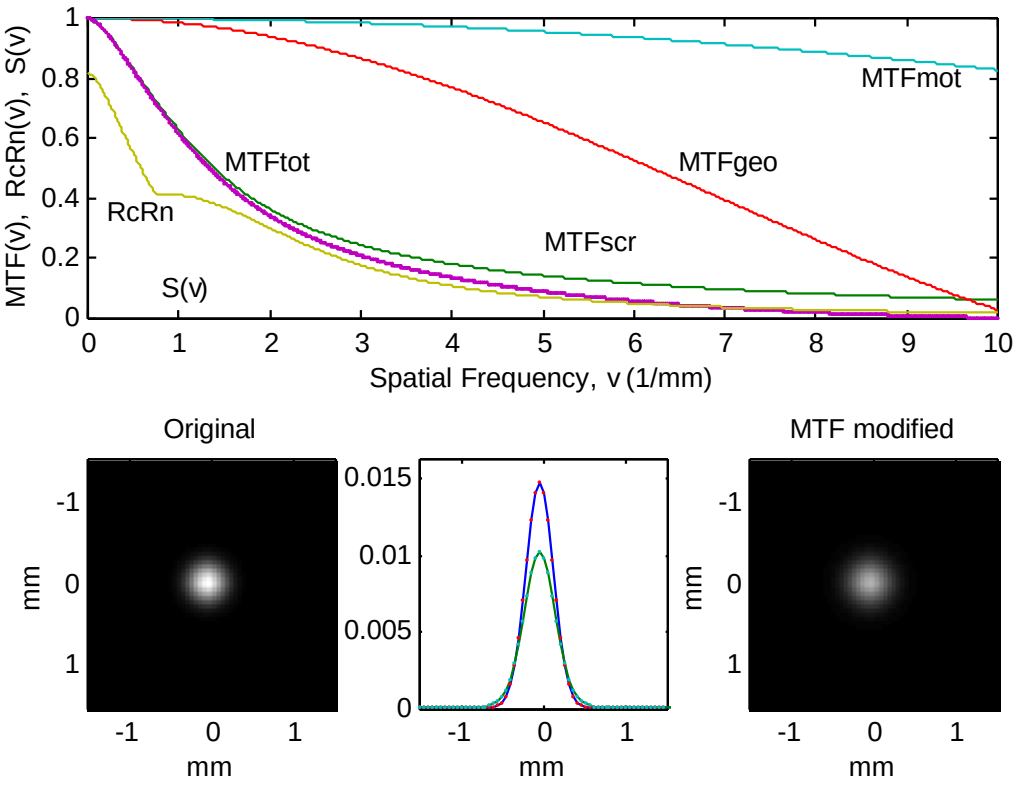

Figure 13. The image to the left shows the original (unmodified) image of a Gaussian-shaped detail with FWHM of 0.5 mm (m=1.11) and the image to the right the MTF-modified image. The figure in the middle shows the profiles through the each centre. In this case the reduction in peak contrast is cdf_{MTF}=0.695. A Kodak Lanex 160 screen, a 'box'-shaped focal spot (f_0=0.9 mm), 20 mm/s motion speed and 3 ms exposure time were used.

3.3. Application to chest and lumbar spine imaging

Our extended model is used below to illustrate the effect of unsharpness on the contrast of small details within a human anatomy. Monte Carlo simulations of chest and lumbar spine imaging systems were performed and the effect of system unsharpness explored. The size and composition of the details included in these examples are given in table 1a and the imaging characteristics are described in table 1b. These were selected from a report by Sandborg *et al.* (1997) that presents measurements of important image details in chest and lumbar spine radiographs. Here only the small details (0.3-1.0 mm) are considered as the influence of the unsharpness on the contrast of the larger details (> 2 mm) is small. The influence of unsharpness is limited to the edges of these structures (blood vessels and spinal processes) and is not considered in this report.

Table 1a. Example of small contrast details included in the voxel-phantom

Chest system	Lumbar Spine system
0.3 mm calcification in left lung apice	0.3 mm bone marrow cavity in spine L3
0.5 mm calcification in left lung apice	0.5 mm bone marrow cavity in spine L3
	1.0 mm bone marrow cavity in spine L3

Table 1b. Imaging system characteristics

Parameter type	Chest system	Lumbar Spine system
Tube potential	141 kV	72 kV
Filtration	5.7 mmAl	3.5 mm Al
Target angle	15°	12°
Focus-film distance	390 cm	146 cm
Focus chest support/couch-top distance	362 cm	134 cm
Air gap	28 cm	12 cm
Chest support/Couch-top	4 mm PMMA (equivalent to 8 mm wood)	0.6 mm Al (equivalent to 6 mm etronite paper)
Grid	No grid	N=52 cm^{-1}, r=10, d=36 μm, 0.155 mm fibre interspace and 0.25+0.25 mm Al covers
Cassette	1.8 mm Mg	1.8 mm Mg
Screen	Kodak Lanex 160	Lanex Regular
Film	Kodak TML	Kodak TML

Figure 14 shows calculated values of ΔOD (difference in optical density behind and beside the detail) of a 0.5 mm thick calcifications in the left lung apices as a function of focal spot size. The diameter of the calcification is either 0.3 or 0.5 mm to explore the effect of differences in spatial-frequency content of details of different size. The optical density beside the detail was 1.57 and the film gradient γ=2.5 (Kodak TML film). The contrast in terms of Monte Carlo calculated values of energy imparted per unit area to the screen, C_ε, was 4.8%. Figure 14a shows that image contrast (ΔOD)

decreases with increasing focal spot size at the larger magnification (m=1.3-1.4), particularly for the smaller detail (fig. 14b). With a small magnification (m=1.05-1.15), the loss in ΔOD is small. This is because the receptor unsharpness is much larger (worse) than the geometric unsharpness (i.e. $MTF_{scr} < MTF_{geo}$). Even if the focal spot size increases it will not significantly change the total unsharpness. It can be noted that for these small focal spot sizes, the contrast increases with magnification. This is because of the increase in size of the detail at the screen-film system with magnification make better use of the limited inherent unsharpness of the screen-film system itself. Magnification shifts higher frequencies in the detail to lower frequencies in the image where MTF_{scr} is higher. A similar but smaller effect on the ΔOD is shown in figure 14a for the larger 0.5 mm calcification.

(a)

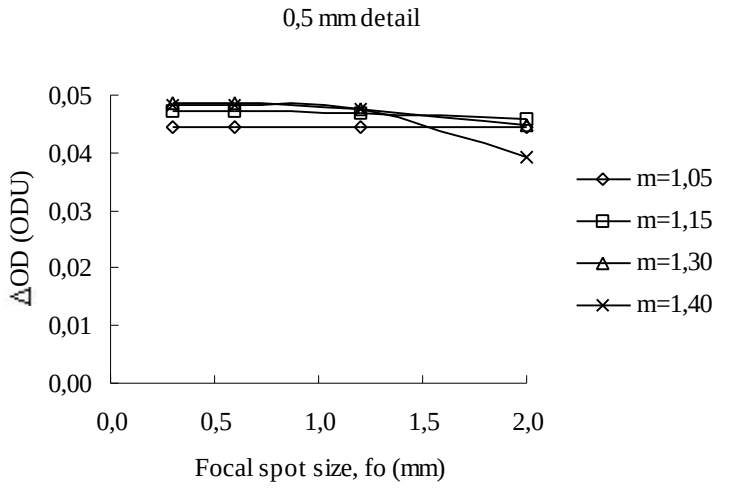

(b)

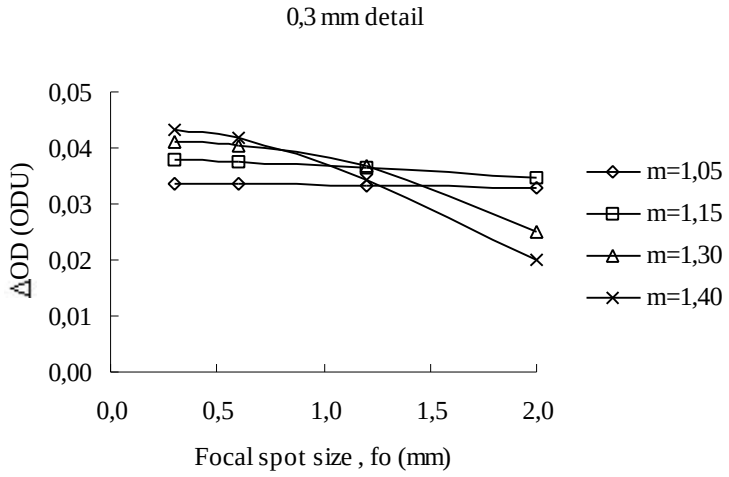

Figure 14. Image contrast, ΔOD, of a 0.5 mm thick calcifications in the left lung apices (a) with a diameter of 0.5 mm and (b) 0.3 mm as a function of the focal spot size at different magnifications. Kodak Lanex 160/TML. Motion unsharpness: 3 ms, motion speed 20 mm/s. A 'box-shaped' focal spot size was used.

Figure 15 shows values of image contrast, ΔOD, of a 1.0 mm bone marrow cavity in the lumbar spine L3 vertebra as a function of focal spot size. The optical density beside the detail being OD_b=1.17. The contrast in terms of energy imparted per unit area to the screen was 3.6%. Three different cavities with different diameters are shown: 1.0, 0.5 and 0.3 mm. With the Kodak Lanex Regular/TML the film gradient is γ=2.4.

The variation with focal spot size and magnification is similar to that in figure 14, as some of the details are of the same size.

(a)

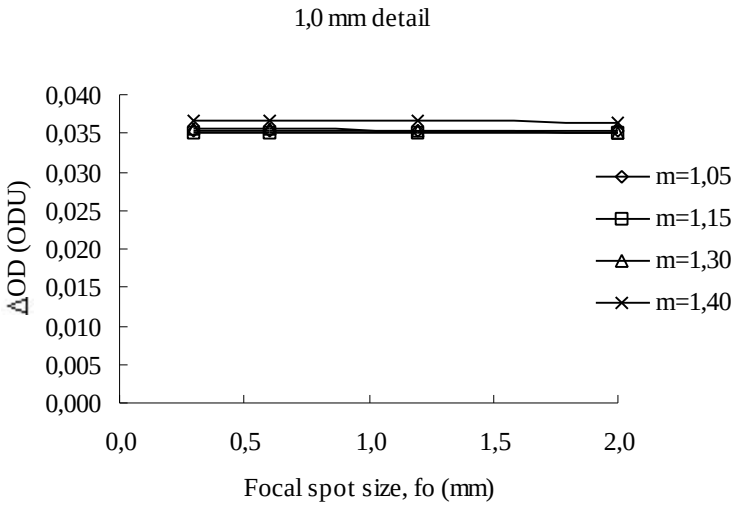

(b)

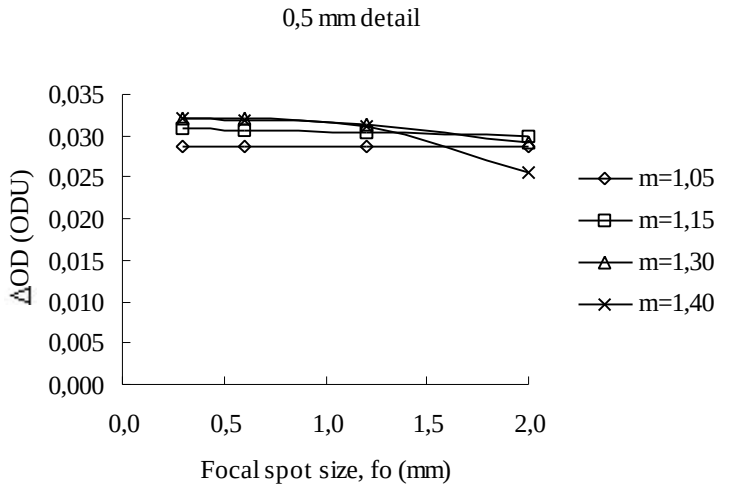

(c)

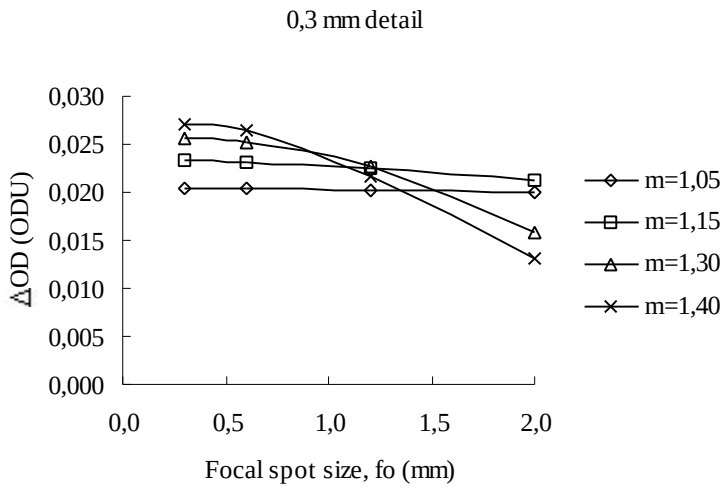

Figure 15. Image contrast, ΔOD, of a 1.0 mm bone marrow cavity in the lumbar spine vertebra L3 but with different diameters (a) 1.0 mm, (b) 0.5 mm and (c) 0.3 mm as a function of the focal spot size ('box-shaped') at different magnifications. Kodak Lanex Regular/TML. No motion unsharpness.

Figures 16-17 show ΔOD of the detail in figures 14a,b and 15b,c expressed as function of the geometric magnification. It is clear that the advantage of magnification is found only when the geometric unsharpness is not the dominating (limiting) source of unsharpness, i.e., at the smallest focal spot sizes (f_0=0.3-0.6 mm) and at low magnifications. For the largest focal spot size (f_0=2.0 mm), a maximum is found at magnifications close to m=1.15-1.20.

(a)

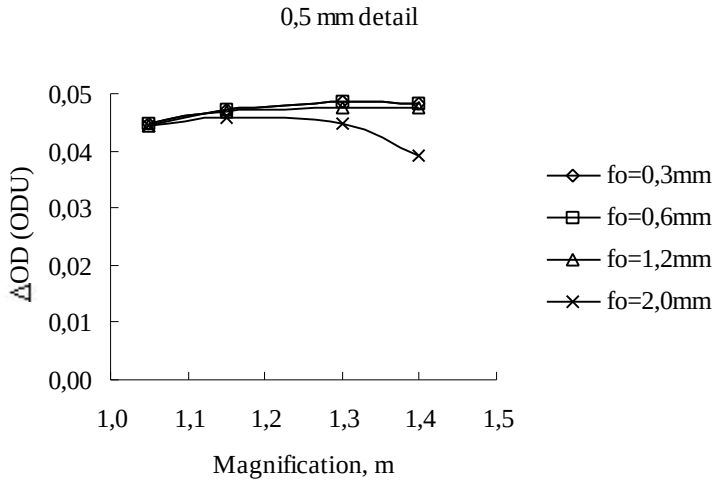

(b)

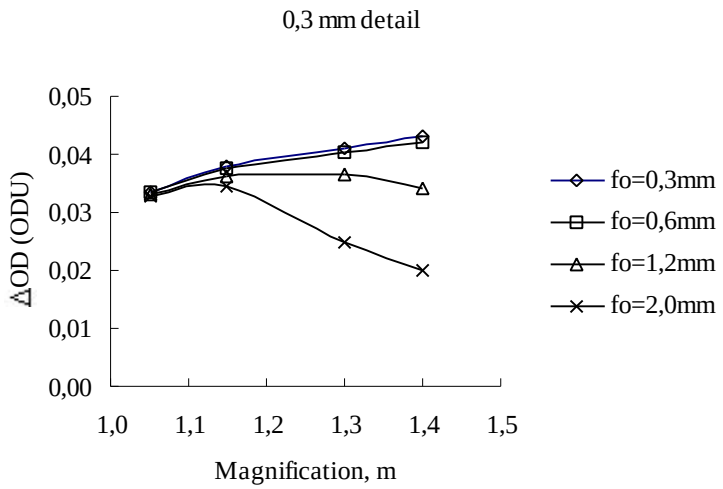

Figure 16. Image contrast ΔOD of a 0.5 mm thick calcifications in the left lung apices for details with (a) 0.5 mm and (b) 0.3 mm diameters as a function of the magnification for different focal spot sizes. Motion unsharpness: 3 ms, motion speed 20 mm/s.

(a)

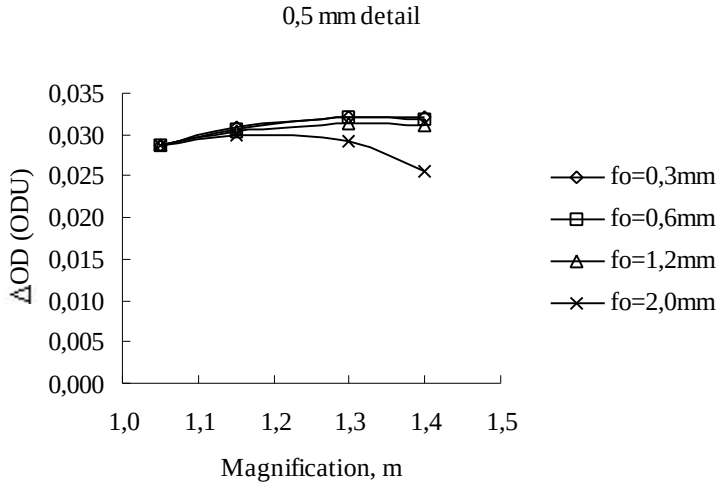

(b)

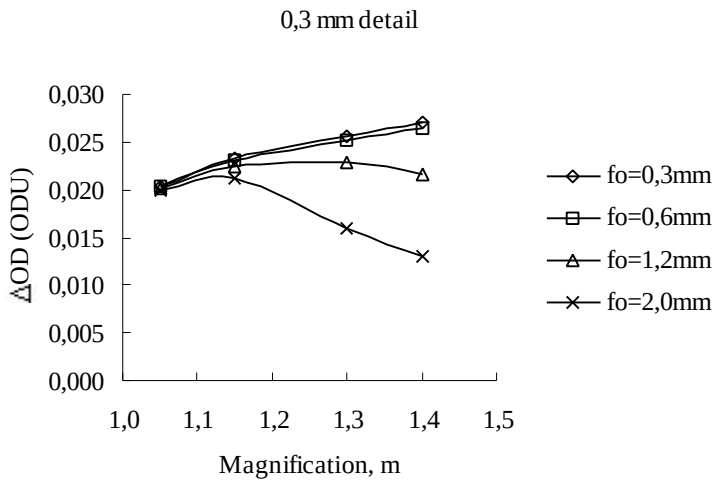

Figure 17. Image contrast ΔOD of a 1.0 mm thick bone marrow cavity in lumbar spine L3 vertebra for cavities with (a) 0.5 mm and (b) 0.3 mm diameters as a function of the magnification for different focal spot sizes. No motion unsharpness.

Figure 18 shows the significant effect of motion unsharpness, MTF_{mot}, on contrast for large motion speed and long exposure times in the chest examination. The comparison is made at magnifications of 1.15 and 1.40. The effect of MTF_{mot} on contrast (ΔOD) is significant only for the longer exposure time (12 ms) and largest magnification (m=1.40); the effect at 3 ms and m=1.15 is only a few per cent. For the large motion unsharpness case (75 mm/s, 12 ms), MTF_{mot} is the limiting component of system unsharpness. The effect of MTF_{mot} is independent of focal spot size but increases with magnification. Therefore, a larger effect of MTF_{mot} is found for small focal spot sizes where the MTF_{geo} is still small. Figure 18 b shows the effect of motion unsharpness for the contrast of a small detail in the lung at increasing motion speed and exposure times. It is shown that for motion speeds up to 50 mm/s and 12 ms exposure time, the effect on motion unsharpness is small and reduces the ΔOD by less than 5%. However, at the maximum motion speed, ΔOD is reduced to less than 60% of its original value.

The effect of motion unsharpness in the lumbar spine examination was not studied due to lack of knowledge of the relevant motion speeds to use but is expected to be small.

(a)

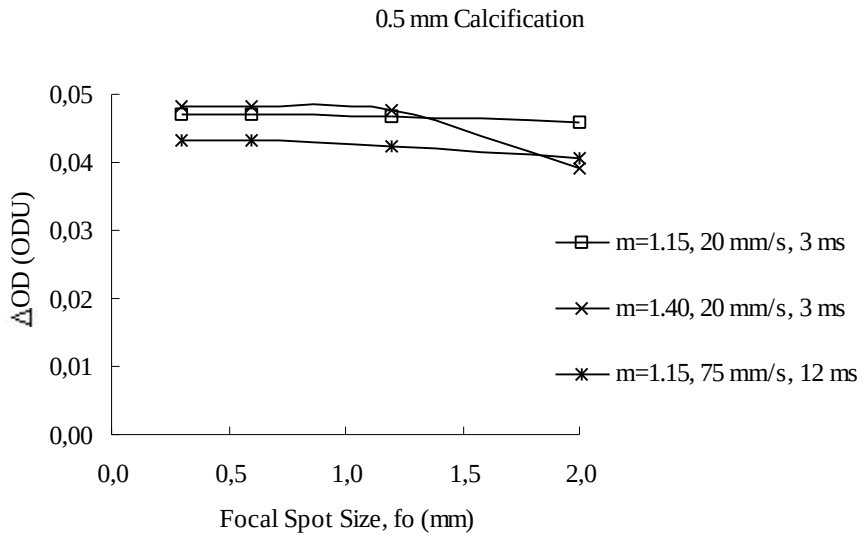

(b)

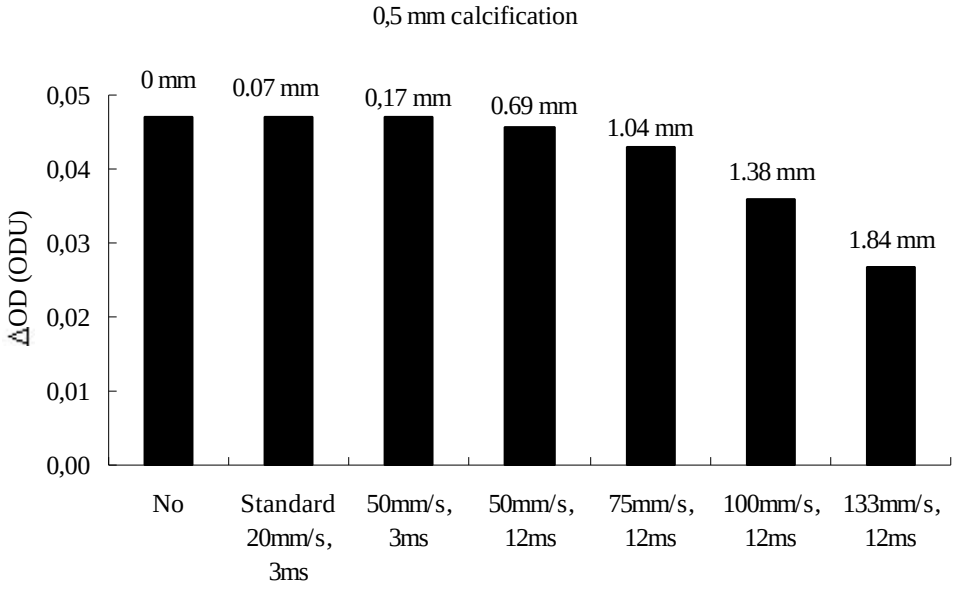

Figure 18. (a) Image contrast ΔOD of a 0.5 mm calcification in the lung apices as a function of the focal spot size at different magnifications and motion unsharpness. (b) Image contrast ΔOD of a 0.5 mm calcification in the lung apices for different combination of motion speed and exposure time. The values printed on top of the histogram bars are the maximum distances the detail can move in the image plane.

4. Noise

Two sources of noise are be considered: screen noise and film noise.

The screen noise (detector noise) can be separated into quantum noise and screen structure noise. Structure noise is due to non-uniform distributions of phosphor grains in the screen-binder emulsion. Very little data on structure noise is available in the literature. Arimura et al. (1996) found that it was less than 15% of the total noise depending on tube potential and optical density, but that it can a larger fraction is some circumstances. Due to lack of data, however, structure noise is not included in the model.

Quantum noise and film noise will be combined using the model of Nishikawa and Yaffe (1990a,b) and their expression for the spatial-frequency dependent detective quantum efficiency, DQE is used in the following. The DQE is a measure of how well the detector transfers the information in the system input to the system output (image). It is defined as the ratio of the squared signal-to-noise ratio, SNR^2_{out} in the detector (output) to that incident on the detector SNR^2_{in}. Four sources of detector inefficiencies are considered here, and each is expressed as a factor between 0-1. The DQE is written:

$$DQE(n,OD) = h \cdot I \cdot R_C(n) \cdot R_N(n,OD) . \qquad (14)$$

The first two factors (η and I) are independent of spatial frequency and are the quantum absorption efficiency, η, and the statistical factor, I. The quantum absorption efficiency is the fraction of the incident photons that interact in the screen. The statistical factor allows for fluctuations in light output at the film and is itself expressed as the product of two factors $I_X \cdot I_L$. The factor I_X arises from variations in the energy imparted to the screen from incident x-ray photons and I_L is due to variations in the number of light photons emitted by the screen and reaching the film emulsion per unit energy imparted to the screen. The I_X can further be divided in to I_{XED} and I_{AED}. The first factor depends on the width of the incident x-ray energy spectrum and the second factor on the fractional absorption of these x-ray photons in the screen. The quantum absorption efficiency, η, and the statistical factor I_X are included in the Monte Carlo model as individual x-ray photons are traced into the screen, but I_L is included separately.

The last two noise-factors (R_C and R_N) depend on the spatial frequency and the latter also on the optical density on the film. R_C is a measure of the different transfer efficiencies of the signal and noise through the screen. For screen-film systems, MTF_{scr} depends on the depth within the screen from which the light is originally emitted. Light emitted close to the film emulsion reduces MTF_{scr} less than light emitted further away from the film. This is further complicated by the fact that light emitted far away from the film is more likely to be absorbed before reaching the film and therefore contribute less to image formation; at least when light absorbing dyes are used in the screen material. The factor R_N is the fraction of the

noise power spectrum that is due to quantum noise. It is therefore reduced from 1.0 when the film noise power is comparably large, i.e., at low and high optical densities and at high spatial frequencies where the quantum noise is blurred.

The inclusion of the statistical factor I_L in the model is described in section 4.1 and the methods used to include the spatial-frequency dependent factors R_C and R_N in the model are described in section 4.2.

4.1. Noise due to the emitted light photons, I_L

4.1.2. Implementation

Whereas the statistical factor I_X, has a strong dependence on the x-ray photon energy, the statistical factor I_L has a much smaller energy dependence, at least for photon energies commonly found at the screen-film system (Swank 1973), Dick and Motz 1981). Some data is available on I_L for Gd_2O_2S phosphor screens (Drangova and Rowlands 1986, Mickish and Beutel 1990 and Ginzburg and Dick 1993). By exposing the screen with photon energies below the K-edge of Gd, measuring the first, and second moments, (M_1 and M_2[#]) of the light distribution and assuming that the statistical factor I_X is close to unity below the K-edge (I_X>0.977: Chan and Doi 1984, Sandborg and Alm Carlsson 1992), I_L has been derived for a Lanex Medium screen (Ginzburg and Dick 1993). Ginzburg and Dick found values of I_L between 0.76-0.81 for 23-50 keV photons (figure 19b). However, Mickish and Beutel (1990) found that I_L is significantly reduced at photon energies below 20 keV (I_L=0.54 at 17.8 keV) (figure 19a). This is due to reduced efficiency in the transport of light to the film from depths in the screen furthest away from the film. Model calculations (Nishikawa et al. 1989, Sandborg *et al*. 1996) indicate that light absorbing dyes and lack of reflective backing in the screen will also reduce I_L.

[#] $M_i(l) = \int_0^\infty l^i f(l) dl$, i = 1, 2 and l is the quantity in consideration, i.e., emitted light energy

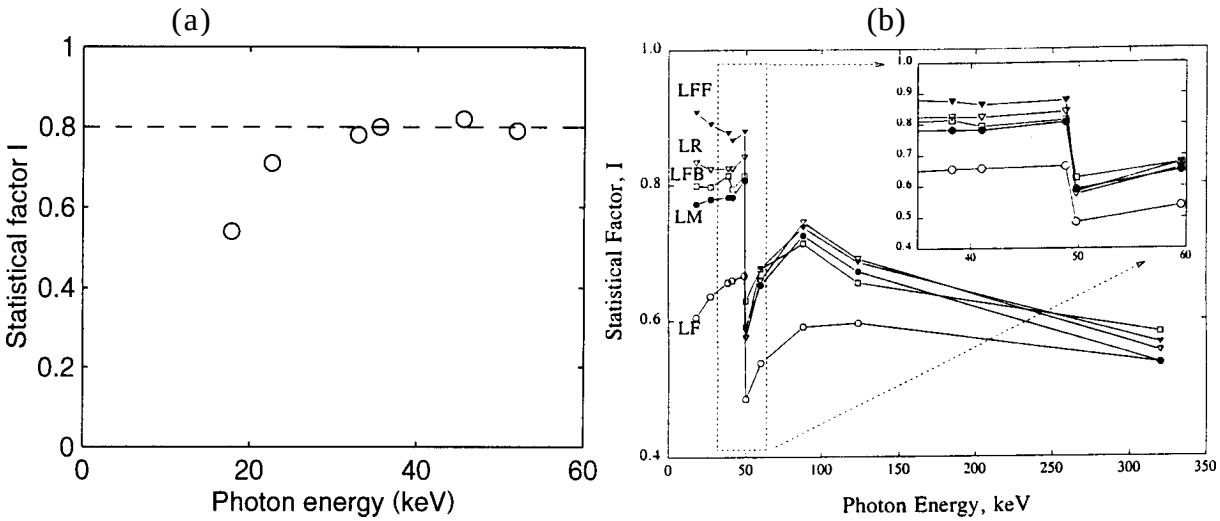

Figure 19. The statistical factor I as function of photon energy for Gd_2O_2S screens. The figure to the left shows data from Mickish and Beutel (1990) and the figure to the right is taken from Ginzburg and Dick (1993) for Kodak Lanex Gd_2O_2S screens. The abbreviations in the figure to the right are: LF, Lanex Fine; LM, Lanex Medium; LFB, Lanex Fast back screen; LFF, Lanex Fast front screen; and LR, Lanex Regular. The K-edge of Gd is located at 50.2 keV. Due to the escape of K-photons, the statistical factors I_X and $I=I_XI_L$ are reduced significantly above this energy. Below 50 keV, I_X is close to 1.0 and $I \approx I_L$.

4.1.2. Application

Models of the transport of light within the screen to the film are available (Swank 1973, Nishikawa and Yaffe 1990, Sandborg *et al*.1996) but are not included here as the variation of I_L with photon energy and screen construction is small for screens typically used in chest and lumbar spine radiography. Such models can therefore be regarded as unnecessarily complicated for our present purposes. Since it is unlikely that photons with energy below 25 keV will contribute much to the energy imparted to the screen (due to their attenuation in the patient, grid and cassette front) a value $I_L=0.80$ will be used for Gd_2O_2S screens at all energies.

4.2. Spatial-frequency dependent factors, R_C and R_N

The last two factors in the DQE expression, R_C and R_N, are both dependent on the spatial frequency, ν. The factor R_N also depends on optical density. The factor R_C is a measure of the different transfer efficiencies of the signal and quantum noise through the screen due to different contributions to detector unsharpness MTF_{scr} from the light emitted from different depths in the screens. The factor R_N is the fraction of quantum noise, NPS_Q, to the total system noise, NPS_T; the total noise being the sum of quantum and film noise.

R_C is defined (Nishikawa and Yaffe 1990a) as

$$R_C(n) = \frac{MTF_{scr}^2(n)}{NTF_Q^2(n)} \tag{15}$$

where

$$\mathrm{NTF}_Q^2(n) = \frac{NPS_Q(n)}{NPS_Q(0)} \tag{16}$$

NTF_Q is called the quantum noise transfer factor and is the quantum noise power spectrum normalised at zero spatial frequency, ν=0 mm^{-1}. MTF_{scr} is the screen-film modulation transfer function. It is here assumed that

$$MTF_{scr} = MTF_{scr+film} \tag{17}$$

i.e., the film unsharpness is negligible compared to the screen unsharpness.

The factor R_N is defined (Nishikawa and Yaffe 1990a) by

$$R_N(n, OD) = \frac{NPS_Q(n, OD)}{NPS_T(n, OD)} = \frac{NPS_Q(n, OD)}{NPS_Q(n, OD) + NPS_F(n, OD)} \tag{18}$$

where NPS_F is the film noise power spectrum and OD is the optical density. It is therefore important to know the relative fractions of film noise (NPS_F) and quantum noise (NPS_Q) as a function both of spatial frequency and optical density.

4.2.1. Implementation

The measured NPS_T was normalised to the NPS_T at a low spatial frequency. Ideally it should be normalised at ν=0 mm^{-1}, but due to suspected inaccuracy in (or difficulty in obtaining) the measured NPS between 0-0.5 mm^{-1}, the NPS was normalised at 0.5 mm^{-1}.

It is common to assume that quantum noise and film noise are additive. To obtain the measured quantum noise power spectrum, NPS_Q, the film noise power spectrum, NPS_F, needs to be subtracted from the total noise power spectrum, NPS_T. From Doi *et al.* (1986) values of the fraction of NPS_F to NPS_T were derived for a range of screen-film systems of different sensitivity (with green sensitive film) at an optical density of 1.0. The fraction of film noise power to total noise power is illustrated in figure 20 as function of spatial frequency.

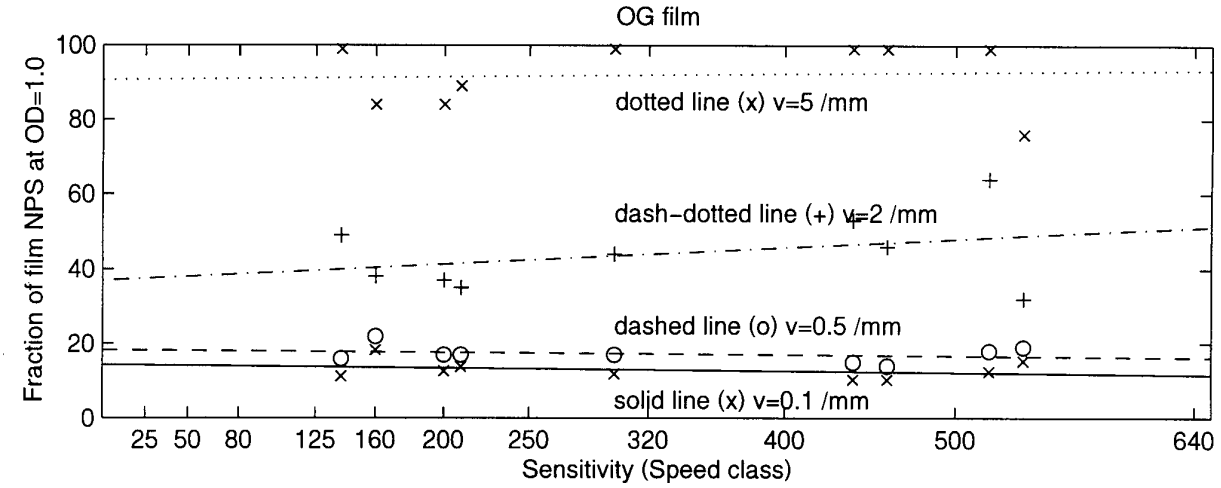

Figure 20. The fraction of film noise power, NPS_F to total screen-film system NPS_T (NPS_Q+NPS_F) noise power as function of screen-film system sensitivity at an optical density of 1.0 and at spatial frequencies of 0.1, 0.5, 2 and 5 mm^{-1}. (Data from Doi *et al.* 1986).

No strong correlation with screen-film sensitivity could be found. The average relative film noise fraction (NPS_F/NPS_T) at different spatial frequencies, $f_F(\nu)=NPS_F/NPS_T$ at speed class 160-600 found are listed in the table below.

ν (mm^{-1})	0.1	0.5	2	5	6	7	8	9	10
$f_F(\nu)$	0.14	0.19	0.40	0.80	0.85	0.87	0.89	0.91	0.92

Hence the NPS_Q was calculated as

$$NPS_Q = NPS_T - f_F NPS_T \qquad (19)$$

The relative fractions of NPS_Q and NPS_F also vary with the optical density. It is therefore necessary to consider the different variations with optical density of the NPS_Q and NPS_F. Selwyn (1935) found that the film noise increases with the square root of the optical density. The film noise relative to that at OD=1.0 therefore changes in relation to

$$NPS_F \sim \sqrt{OD_{det}/1.0} \qquad (20)$$

where OD_{det} is the optical density beside the contrasting detail for which the signal-to-noise ratio is to be calculated. Figure 21 compares the measured NPS_F with a model assuming a square-root dependence with optical density. This model works and will be used to scale the NPS_F with the optical density.

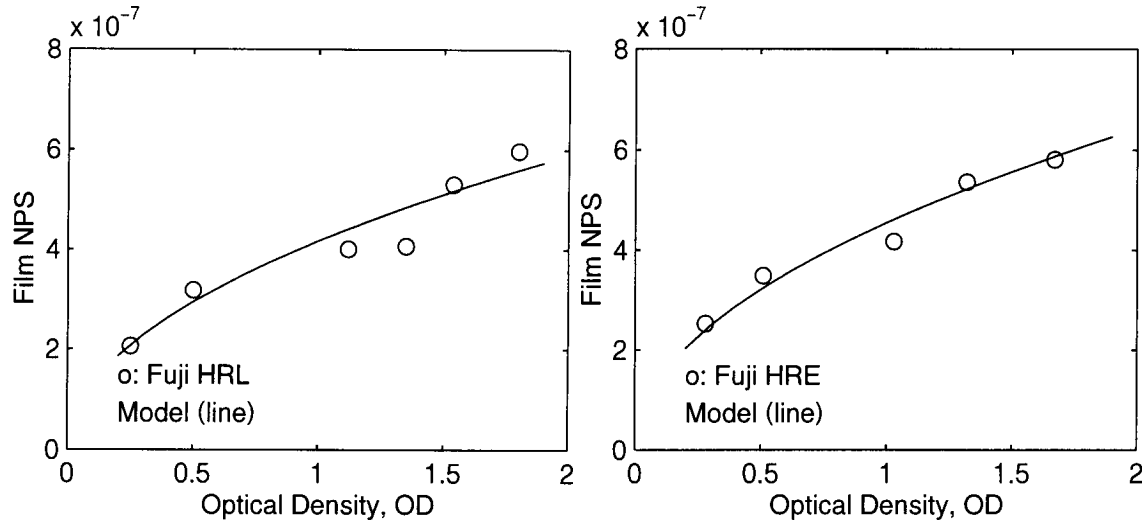

Figure 21. Comparison of measured NPS_F as a function of the optical density on the film with values of the model that assumes that the NPS_F increases as $OD^{0.5}$ (Selwyn 1935). The film Fuji HRE and HRL were used. For the measured NPS_F it was assumed that at a spatial frequency interval between 20-22 mm^{-1} of the total noise NPS_T (Verdun, personal communication), NPS_F is the only remaining noise. In this region quantum noise NPS_Q is negligible due to its strong dependence on MTF_{scr}.

The quantum noise power spectrum increases as the film gradient squared and decreases inversely with the number of absorbed photons in the screen. For a given x-ray spectrum, the optical density is approximately proportional to the number of absorbed photons in the screen and approximated with the energy imparted to the screen. (This approximation is only used here in obtaining the correction factor for the SNR and not used in calculating the quantum noise or the SNR itself in the Monte Carlo model). The quantum noise relative to that at OD=1.0 therefore changes by

$$NPS_Q \sim \left[g(OD_{\det})^2 \cdot e_{scr}(1.0) \right] / \left[g(1.0)^2 \cdot e_{scr}(OD_{\det}) \right] \qquad (21)$$

The contributions of the film, NPS'_F and quantum noise NPS'_Q at OD_{det} are thus

$$NPS'_F = NPS_F \cdot \sqrt{OD_{\det}/1.0} \qquad (22)$$

$$NPS'_Q = NPS_Q \cdot \left[g(OD_{der})^2 \cdot e_{scr}(1.0) \right] / \left[g(1.0)^2 \cdot e_{scr}(OD_{\det}) \right] \qquad (23)$$

and the total noise, NPS'_T at OD_{det}

$$NPS'_T = NPS'_Q + NPS'_F \qquad (24)$$

These expressions were used to calculate the R_N factor at different optical densities; the R_C factor being independent of optical density.

4.2.2. Application

Figure 22 shows the noise power spectra components as a function of the spatial frequency for the Lanex Medium and Curix Medium screen-film systems. The NPS_Q drops much faster than the NPS_F with increasing spatial frequency.

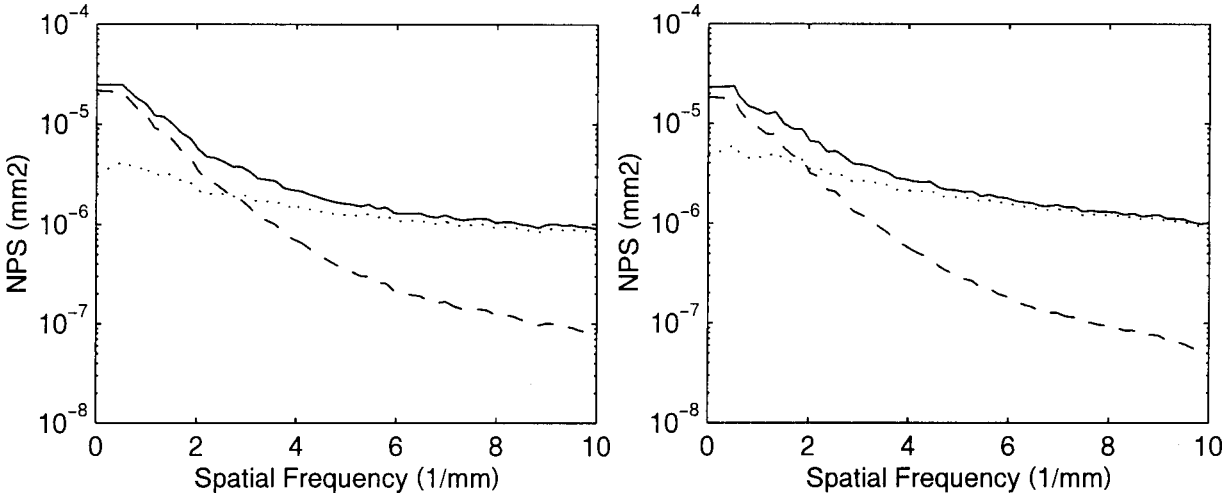

Figure 22. The noise power spectra NPS_T (——), NPS_Q (- - -), and NPS_F (.....) at an optical density of 1.3 and 1.4 for Lanex Medium (left) and Curix Medium (right), respectively. (Values of NPS_T were obtained from Verdun et al, personal communication 1997).

Figure 23 shows the frequency spectra of the factors R_C and R_N and their variation with spatial frequency. Both factors decrease with increasing spatial frequency. The R_C factor is different for the two screens; the factor for Curix Medium being much lower. There is an error associated with R_C due to the uncertainty in the measured NPS at low frequencies. As a consequence, at the lower spatial frequencies, R_C in figure 23 takes values above one. This is inconsistent with the model and must be due to uncertainties or noise in the measured values of NPS and MTF.

There is also an error associated with values of R_N because no measurements of film noise have been made. The magnitude of film noise has been derived as an average of data from the literature (see description above). Therefore, the fraction of film noise is the same for both Fuji and Kodak films in this report.

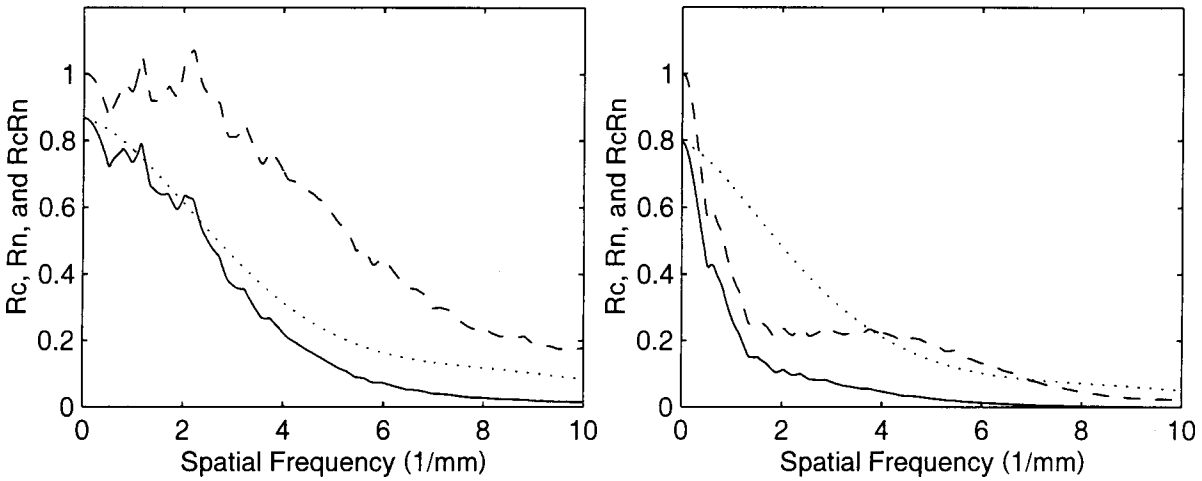

Figure 23. The calculated factors $R_C \cdot R_N$ (——), R_C (- - -), and R_N (.....) at an optical density of 1.3 for Lanex Medium (left) and 1.4 for Curix Medium (right).

Figure 24 shows the fraction of film to total noise as a function of optical density at different spatial frequencies. The film noise is a large fraction of the total noise at low and high optical densities and its fractional contribution increases with increasing spatial frequency. However, the quantum noise dominates for optical densities between 0.5-2.5 at spatial frequencies less than 2 mm^{-1}. The fraction of film to total noise is equal to $1-R_N$.

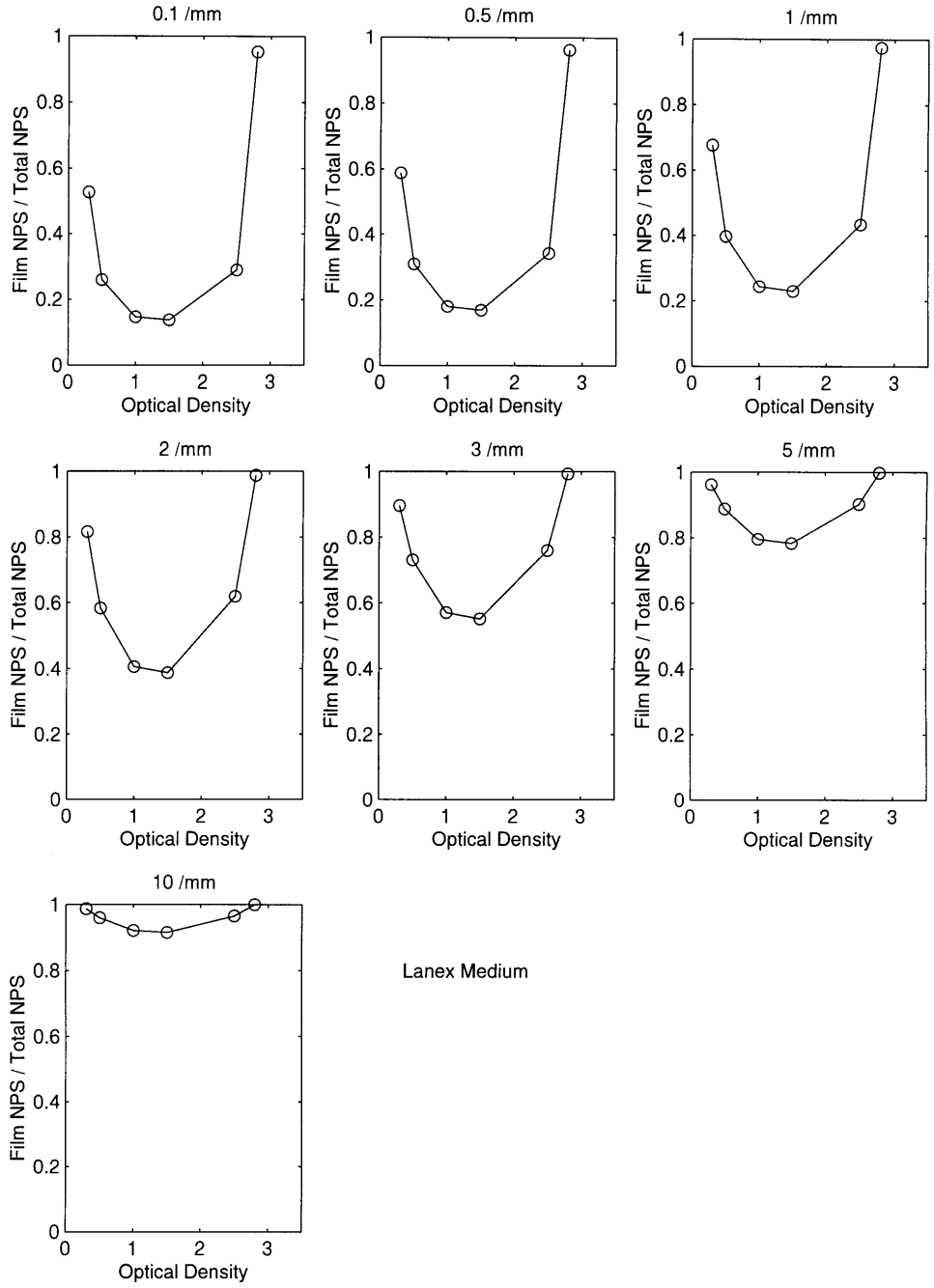

Figure 24. The ratio of film to total noise NPS_F/NPS_T as function of the optical density on the film for spatial frequencies: 0.1, 0.5, 1.0, 2,0, 3.0, 4.0 and 10.0 mm^{-1}. A Lanex Medium / Fuji HRE screen-film system was simulated.

4.3. Other sources of noise

4.3.1. "Anatomical noise"

"Anatomical noise" is not noise in the same sense as screen-film noise, but manifests itself in a similar way to interfere with the detection of the detail of interest. Some of the small variations in optical density on the film are due to small variations in tissue density and tissue composition in the 'normal' tissue texture. Although important, anatomical noise is not included in the model due to lack of data.

5. Signal-to-noise ratio, SNR

5.1. The ideal observer SNR_I

Statistical decision theory provides the means for defining and measuring image quality as related to the achievable performance in a given imaging task. Due to difficulty in knowing the actual signals to be considered in clinical images, most studies are performed on a 'signal known exactly' where the task is to detect this known signal in a noisy background. For low-contrast details, the noise is signal-independent and normally distributed and the image quality (i.e. the image information as related to the detectability of the detail) can be expressed by the SNR of the best possible (ideal) observer, SNR_I. ICRU (1996) expresses the SNR_I as the product of the diagnostic task $\Delta S(\nu)$ and the noise equivalent quanta, $NEQ(\nu)$ (Dainty and Shaw 1974) such that

$$SNR_I^2 = \int |\Delta S(n)|^2 \cdot NEQ(n) d^2 n = \int \frac{|\Delta S(n)|^2 \cdot g^2 \cdot MTF^2(n)}{NPS(n)} d^2 n \ . \quad (25)$$

Tapiovaara and Sandborg (1995) compared measured and calculated values of the SNR using measurement and calculation procedures described in Tapiovaara (1993) and Sandborg *et al*. (1994), respectively. The signal-to-noise ratio derived from the Monte Carlo simulation, SNR_{MC} was calculated using

$$SNR_{MC}^2 = \frac{\left| E(l_1)E(n_{p,1}) - E(l_2)E(n_{p,2)} \right|^2}{\left[E(l_1^2)E(n_{p,1}) + E(l_s^2)E(n_s) \right]} \quad (26)$$

where the signal in the numerator is given by the difference in the energy imparted to the image detector in the shadow area of the detail ($E(l_i)E(n_{p,i}) = E(e_{p,i})$), without ($i$=1) and with ($i$=2) the detail present; index s indicates corresponding values for the scattered photons (assumed to be independent of the presence of the detail). E(n) is the mean (expectation value) of the number of photons incident on the detector and λ is the energy imparted to the detector by an incident photon and its associated secondary particles. The expectation values $E(\lambda)$ and $E(\lambda^2)$ are the first and second moments, respectively, of the energy imparted to the detector per incident photon.

This expression ignores the frequency dependence of the NEQ and assumes a sharp system with white noise and is therefore only applicable for large-area contrast details with a narrow signal-spectrum. SNR_{MC}^2 is proportional to the area of the detail. For small details the signal spectrum is wider and $MTF^2(\nu)/NPS(\nu)$ decreases at higher frequencies. The SNR^2 of small objects therefore decreases faster with decreasing object area than the simple proportionality to detail area would suggest (Wagner and Brown (1985). An example of this is given in figure 25 where the results of measurement and calculation of SNR_I^2 are compared. The comparison was made using a x-ray image intensifier system (Philips Imagica HC 23 cm). In this

figure, the SNR_I^2 of details of a given thickness but of increasing area are shown. There is a good agreement between the calculated and measured values for the details with diameter larger than or equal to 3 mm. For the smaller details, however, the simple expression above for the calculated values (SNR^2_{MC}) overestimates the SNR_I^2 by about 30% (1 mm diameter), hence the need to include the frequency-dependent R_C factor into the model.

The values shown in figure 25 were, before being plotted, corrected for the statistical factor I_L (calculations) and for video noise (measurements). The corrections were made as follows. The calculated values SNR^2_{MC} were multiplied by the factor I_L=0.95 to allow for the small variation in the light pulses at the output of the CsI screen. The fraction of video (non-quantum) noise was measured and was found to be between 1-7% (depending on optical aperture size and video amplifier gain). Hence, the measured values of SNR^2 were multiplied by a factor 1.01-1.07 to allow for this additional noise. Both these corrections are small, but when applied, allowing comparison between measured and calculated values of SNR^2 on an absolute scale.

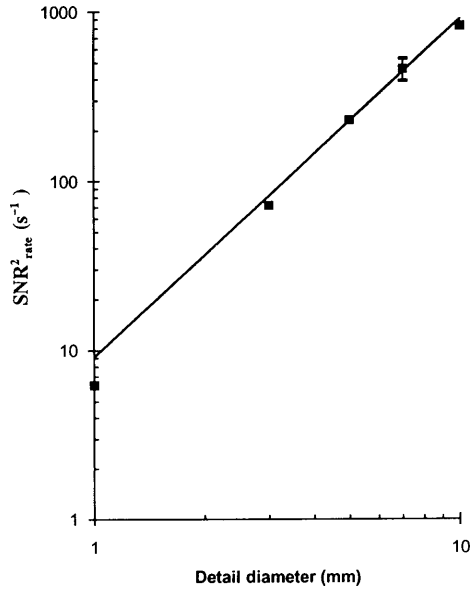

Figure 25. The SNR^2 for detecting a 3 mm thick plexiglas (PMMA) details, as a function of the detail diameter. X-ray tube potential 51 kV, total filtration 22.7 mm Al. Monte Carlo calculation (solid line); ■ measurement. (From Tapiovaara and Sandborg 1995).

Figure 26 shows results from additional comparisons made between calculated and measured values of SNR^2. Plexiglas (PMMA) phantoms and low-contrast details of either plexiglas or iodine were used. The x-ray tube potential, filtration and scatter-rejection technique were varied. The results were described by the dose-to-information conversion factor, $SNR^2/\overline{D}$. Figure 26a shows the results, on an absolute scale, for a 3 mm thick and 10 mm diameter plexiglas contrasting detail.

Both the shape and the numerical values of $SNR^2/\overline{D}$ agree within measurement errors. These results indicate that all major inefficiencies of the imaging system are included in the Monte Carlo model, except for video noise. In figure 26b, comparison is made on a relative scale, since the iodine contrast details were of uneven and unknown thickness. These results show that the effect of the atomic composition of the detail is similar in the calculated and measured data and that the dependence on x-ray spectrum and scatter-rejection technique is properly modelled. The model is thus able to show that the most efficient combination (of those considered) to use is 60 kV tube potential, additional copper filtration and a fibre anti-scatter grid.

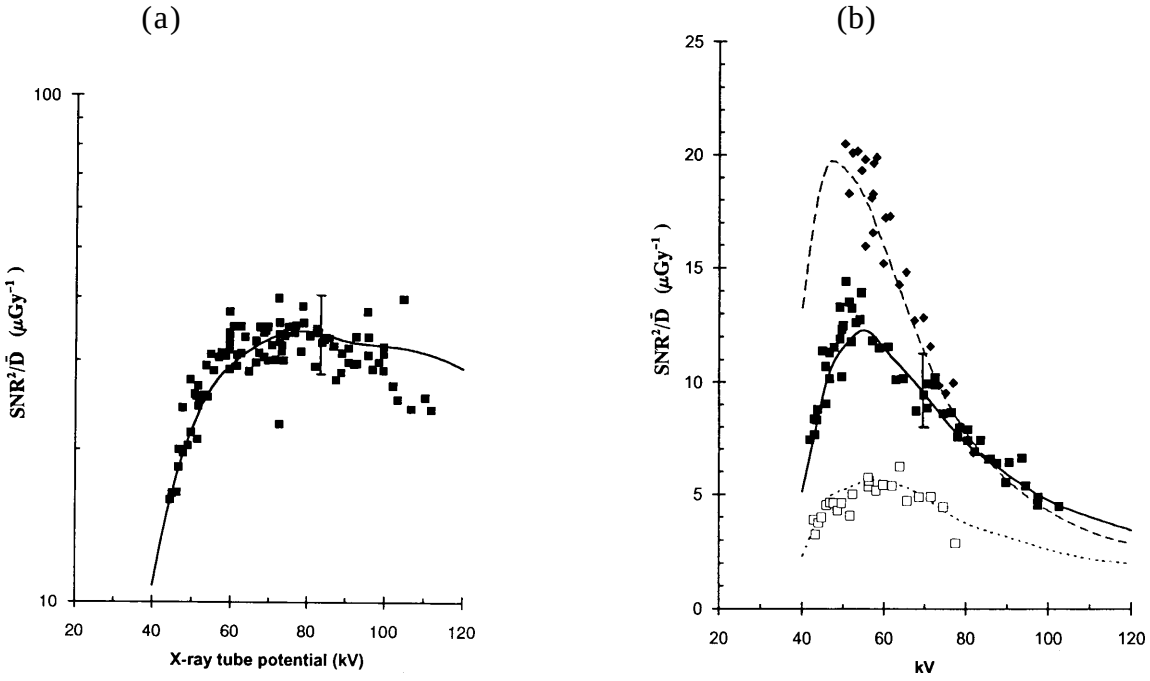

Figure 26. (a) Measured and calculated dose-to-information conversion factors, $SNR^2/\overline{D}$ for detecting a 10 mm diameter (thickness 3 mm) disk detail added to a 20 cm thick PMMA phantom, as a function of the tube potential. A fibre grid was used. The error bar shows two standard deviations of the measured data. The standard deviation of calculated and measured data are 3.5% and 7.5%, respectively. The calculated data were corrected for I_L=0.95 and the measured data for video noise (1-7% of total noise). (b) Relative $SNR^2/\overline{D}$ for detecting a low-contrast iodine detail. The upper two curves and data points are for imaging with a fibre grid (N=44 cm^{-1}, r=10, 36 μm lead strips, 1.0 mm cover), and the lowest curve and data points for imaging without a grid. Fibre grid, 2.7 mm Al filtration (solid line and ■), fibre grid, 2.7 mm Al and 0.25 mm Cu filtration (dashed line and ◆), and no grid, 2.7 mm Al filtration (dotted line and □). The data was normalised at 70 kV and no grid. (From Tapiovaara and Sandborg 1995).

Our Monte Carlo derived values of SNR_I^2 , for use in this work are based on the expression for SNR_{MC}^2 described briefly above (and in more detail in Tapiovaara and

Sandborg (1995)). Correction factors are, however, needed as SNR_{MC}^2 does not consider the spatial-frequency dependence of the NEQ (R_C), other noise sources (R_N) nor the statistical factor I_L. These corrections are applied to the Monte Carlo derived values of SNR_{MC}^2 using the following strategy.

5.2. Implementation of correction factors to Monte Carlo calculated SNR_{MC}

The reduction in SNR^2 due to screen and film noise and of unsharpness is here quantified by the so-called SNR^2 degradation factor, $SNRDF^2$ defined as

$$SNRDF^2(OD_{\det}) = I_L \cdot \frac{\int_v \Delta S^2(n) \cdot MTF_{mot}^2(n) \cdot MTF_{geo}^2(n) \cdot R_C(n) \cdot R_N(n, OD_{\det}) \cdot dn}{\int_v \Delta S^2(n) \cdot dn} . \quad (27)$$

$\Delta S(\nu)$ is the contrasting detail's spatial-frequency spectrum for a given size and shape and MTF_{mot} and MTF_{geo} are the motion and geometric unsharpness functions. These two MTFs introduce a loss of SNR due to coupling of the signal to other signals and to noise but not between individual noise events (Sandrik and Wagner 1982), hence the geometric and motion unsharpness reduce the signal but not the noise. The influence of screen-film unsharpness MTF_{scr} is included in R_C and the influence of film noise is included in R_N. The weighting of the imaging system characteristics (R_C, R_N, MTF_{mot} and MTF_{geo}) with $\Delta S(\nu)$ indicates that the degradation factor ($SNRDF^2$) is calculated separately for each imaging task (contrast-detail). The statistical factor I_L has been described previously.

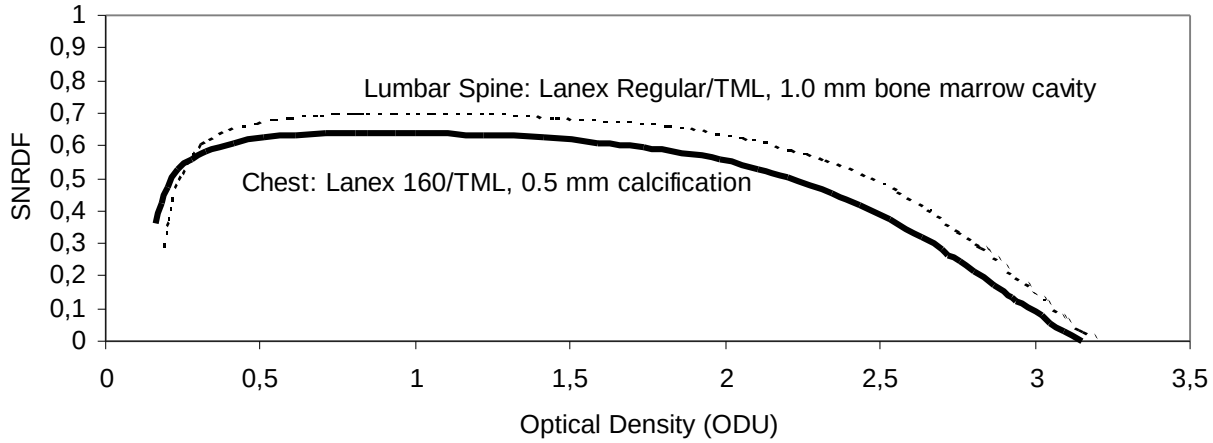

Figure 27. The SNRDF as function of optical density beside the detail for two imaging situations and imaging tasks. A chest PA examination with a Lanex 160/TML screen-film system was modelled imaging a 0.5 mm diameter calcification (——) and a lumbar spine AP examination with a Lanex Regular/TML screen-film system imaging a 1.0 mm diameter bone marrow cavity (- - - -).

Figure 27 shows the SNRDF as function of optical density for two imaging situations (chest PA 0.5 mm calcification and lumbar spine AP 1.0 mm bone marrow cavity). The SNRDF is reduced at low and high optical densities because of the lower value of the R_N-factor due to a comparably larger fraction of film noise compared to quantum noise at these optical densities (see figure 24). The reduction from 1.0 is also due to the I_L factor (=0.80) and the R_C factor. The value of the SNRDF-factor is, for OD>0.25, larger for the detail with the larger diameter (1.0 mm detail compared to the 0.5 mm detail). This is due to the reduction of the $R_C R_N$ with increasing spatial frequency (see figure 12a) and the lower amplitude of high frequencies for the larger detail, resulting in a higher $R_C R_N$-value.

The signal-to-noise ratio of the ideal observer, SNR^2_I (ICRU 1996) for detecting a thin contrasting detail displayed with an optical density OD_{det} just beside the detail will be calculated by

$$SNR_I^2(OD_{\text{det}}) = SNR_{MC}^2(e_{\text{det}}) \cdot \frac{A_{\text{det}}}{A_{MC}} \cdot SNRDF^2(OD_{\text{det}}). \qquad (28)$$

$SNR^2_{MC}(\varepsilon_{det})$ is the signal-to-noise ratio from the Monte Carlo simulation for a given area and thickness of the detail and in terms of the energy imparted per unit area to the detector, ε_{det}, just beside the detail. The ratio A_{det}/A_{MC} is the ratio of the area of the detail, A_{det}, to the area used in the Monte Carlo program, A_{MC}, to calculate the SNR_{MC} (A_{MC}=0.25 mm^2).

5.3. Application to chest and lumbar spine imaging

Illustrated below are the effects of unsharpness and added noise on the SNR of the small details within the model human anatomy (Yale voxel-phantom). Monte Carlo simulations of the chest and lumbar spine examinations were performed using the same small low-contrast details and imaging systems as given in table 1a above. The inherent low contrast and small size (area) of these details result in values of SNR that are close to, or below what are commonly recognised as detectable (SNR≈5, Rose 1948) on homogeneous but noisy background. Displayed on the varying background of a normal human anatomy, these details will be difficult to detect due to their low SNR and thus put the imaging system to a difficult test.

Figure 27 (chest) and 28 (lumbar spine) show the effect of focal spot size on the SNR for different magnifications in the chest and lumbar spine examination, respectively. Similarly as for the contrast (Figs. 14-15), the SNR decreases with increasing focal spot size; the decrease being smaller for the larger magnifications as expected. Also the influence on SNR of the focal spot size is larger for the smaller detail due to its wider signal-spectrum.

(a)

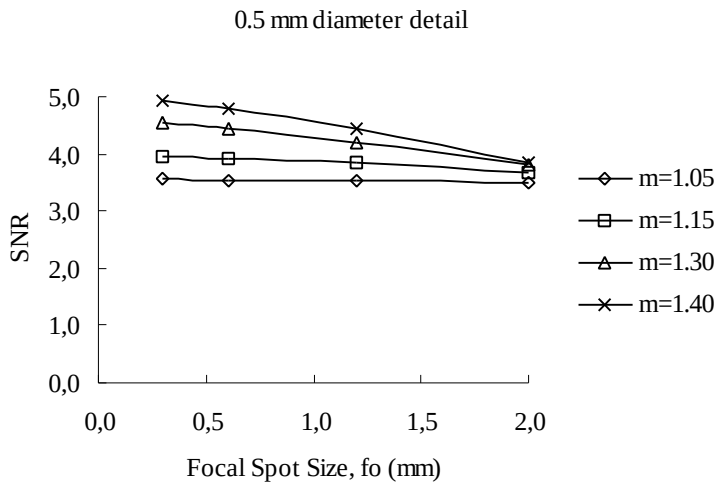

(b)

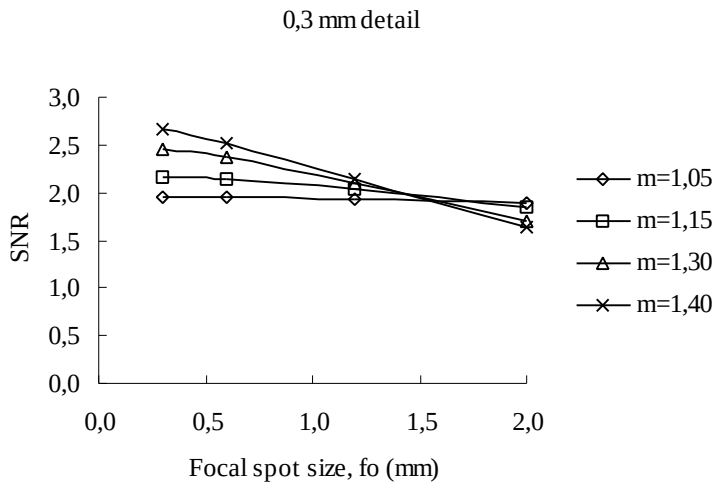

Figure 27. The SNR of a 0.5 mm thick calcifications in the left lung apice as a function of the focal spot size at different magnifications and detail diameters (a) 0.5 mm and (b) 0.3 mm. Lanex 160 /TML, 20 mm/s, 3 ms motion unsharpness. A 'box-shaped' focal spot was simulated.

(a)

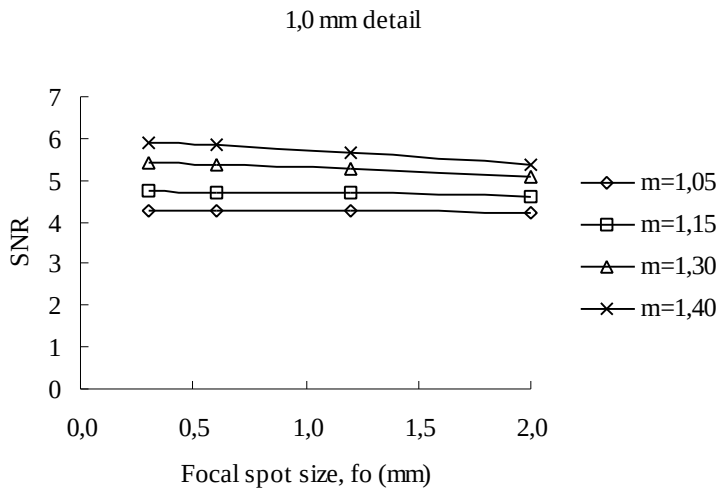
1,0 mm detail
SNR
7
6
5
4
3
2
1
0
0,0
0,5
1,0
1,5
2,0
Focal spot size, fo (mm)
m=1,05
m=1,15
m=1,30
m=1,40

(b)

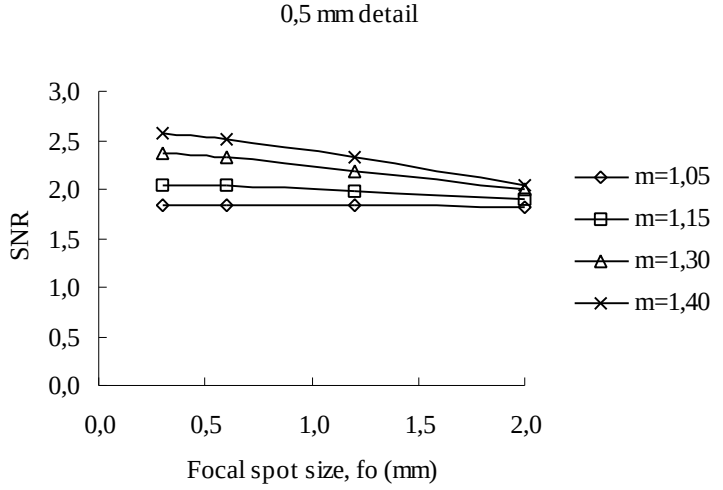
0,5 mm detail
SNR
3,0
2,5
2,0
1,5
1,0
0,5
0,0
0,0
0,5
1,0
1,5
2,0
Focal spot size, fo (mm)
m=1,05
m=1,15
m=1,30
m=1,40

(c)

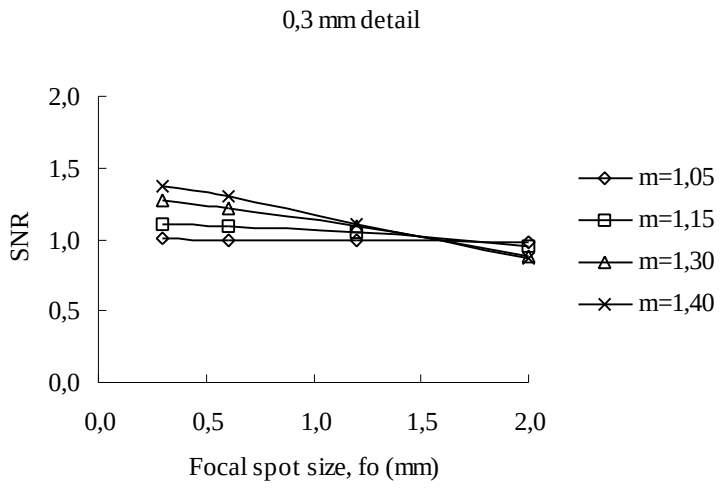

Figure 28. The SNR of 1mm thick bone marrow cavity in the lumbar spine L3 vertebra with different simulated diameter; (a) 1.0 mm (b) 0.5 mm and (b) 0.3 mm as a function of the focal spot size at different magnifications. Lanex Regular/TML, no motion unsharpness. A 'box-shaped' focal spot was simulated.

Figure 29 shows the variation of the SNR with the magnification for different focal spot sizes. For the largest focal spot size (f_0=2.0mm) and the smallest detail (0.3 mm diameter), magnification reduces the SNR, whereas, similarly to the results for contrast, the SNR increases with increasing magnification using the small focal spots. Contrary to the contrast, the SNR increases linearly with the magnification, i.e., with the square root of the detail's area.

(a)

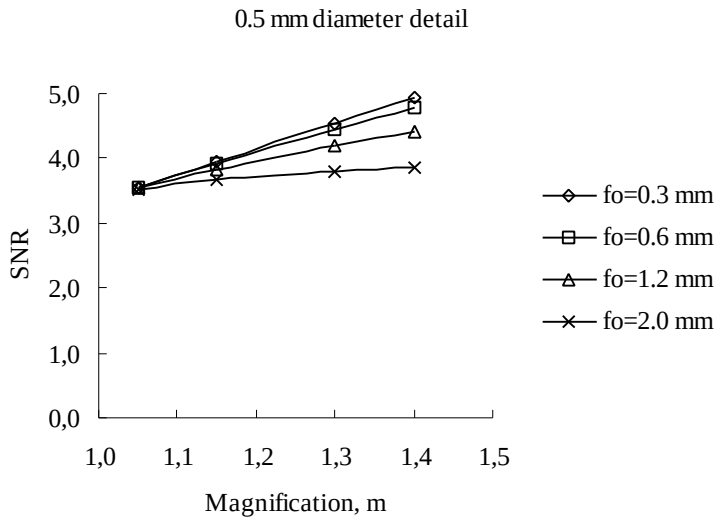

(b)

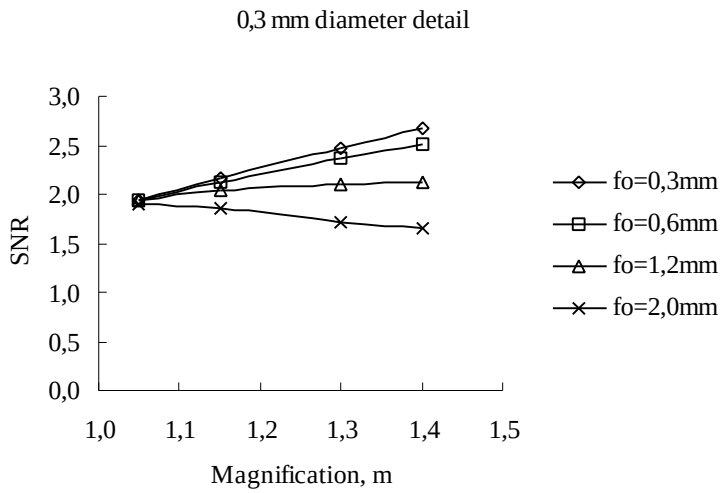

Figure 29. The SNR of a 0.5 mm thick calcification in the left lung apice with different diameter (a) 0.5 mm, and (b) 0.3 mm as a function of the magnification for different focal spot sizes.

(a)

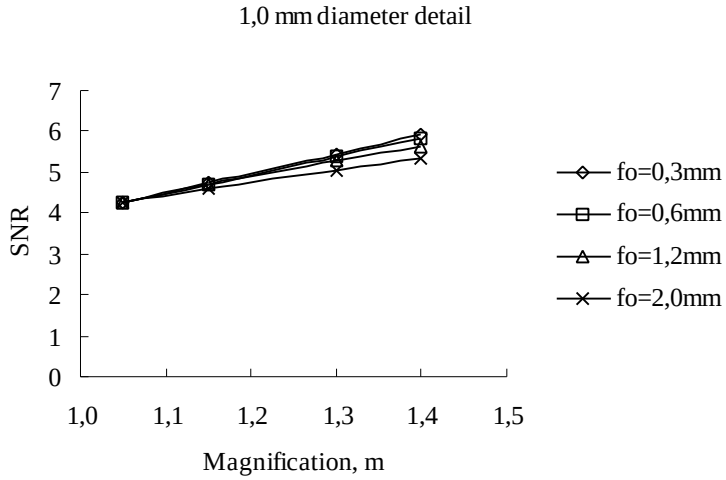

(b)

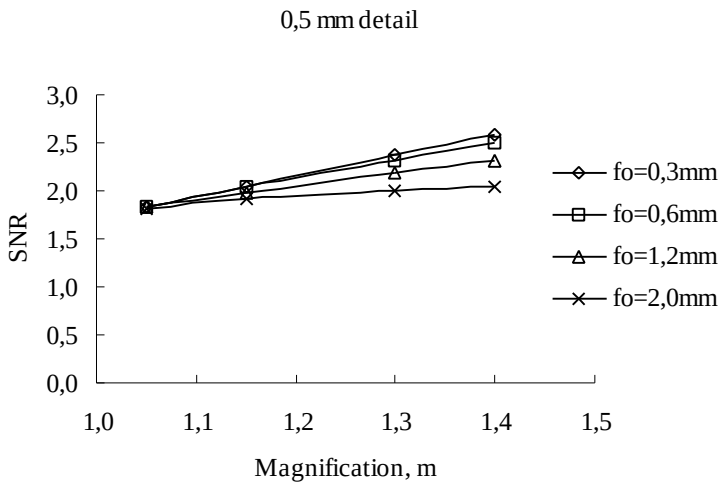

(c)

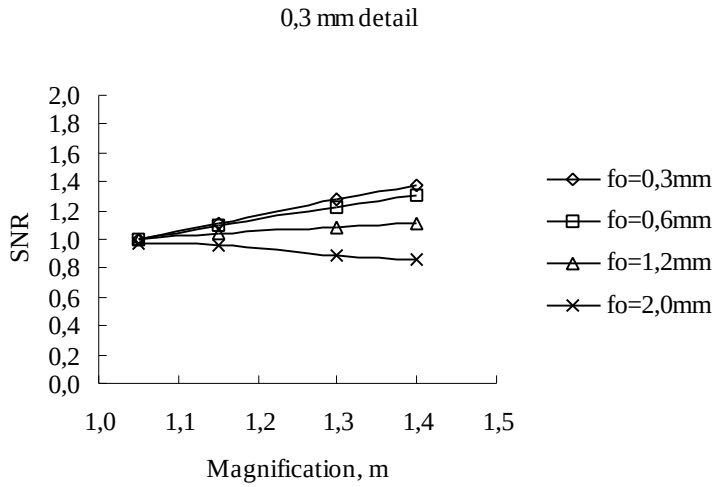

Figure 30. The SNR of a 1.0mm thick bone marrow cavity with diameter (a) 1.0 mm (b), 0.5 mm, and (c) 0.3 mm in the lumbar spine L3 vertebra as a function of the magnification for different focal spot sizes.

6. Conclusion

The objective of this report was to explore the effect of imaging system unsharpness and added detector noise and to calculate correction factors to apply to the results from the Monte Carlo simulation of the complete x-ray imaging system. The Monte Carlo model derives values of the contrast and SNR (of details in the human anatomy) in terms of the energy imparted to the image detector (fluorescent screen) without the influence unsharpness, screen and film noise.

The methods used to implement different sources of imaging system unsharpness and detector noise other than that due to fluctuations in the energy imparted to the detector are described in this report. The correction factors were specifically calculated for each size and shape of the contrasting detail in consideration and for each imaging geometry and image detector. Methods to model geometric and motion unsharpness as well as additional sources of detector noise were taken from the literature.

Acknowledgement
This work was supported by grants from the Commission of the European Communities (FI4P CT950005). MS was also supported by grants from the Swedish Radiation Protection Institute, SSI (SSI P 1018.97), and the Swedish Medical Research Council, MFR (K98-17X-12652-01A).

References

Arimura H, Okamoto M, Nakamori N, Kanamori H, Kubota H, Matsumoto M, Takigawa A, X-ray tube voltage dependence of Wiener spectra of quantum mottle obtained by determining detective quantum efficiencies of a screen *Opt. Eng.*, **35**, 926-937, 1996

Carmichael J H E, Maccia C, Moores B et al M European guidelines on quality criteria for diagnostic radiographic images EUR 16260 EN, (Luxembourg, 1996)

Chan HP and Doi K, Studies of x-ray energy absorption and quantum noise properties of x-ray screens by use of Monte Carlo simulation *Med. Phys.*, **11**, 37-46, 1984

Chaney E L and Hendee W R, Effects of x-ray tube current and voltage on effective focal-spot size *Med. Phys.*, **1**, 141-147, 1974

Dainty J C and Shaw R, *Image Science* (London, Academic 1974)

Dance D R, Persliden J, and Alm Carlsson G, Calculation of dose and contrast for two mammography grids *Phys. Med. Biol.*, **37**, 235-248, 1992

Dick C E and Motz J W, Image information transfer properties of x-ray fluorescent screens *Med. Phys.* **8**, 337-346, 1981

DIN 6867, Teil 2. Bildregistrierendes System Bestehend aus Röntgenfilm, Verstärkungsfolien und Kassetten zur Verwendung in der medizinischen Röntgendiagnostik. Deutsches Institut für Normung e.V., April 1985.

Doi K, Kodera Y, Loo L-H, Chan H-P, Higashida Y, Jennings R J, MTF's and Wiener spectra of radiographic screen-film systems Volume II HHS Publ. FDA 86-8257, 1986

Drangova M and Rowlands J A, Optical factors affecting the detective quantum efficiency of radiographic screens *Med. Phys.*, **13**, 150-157, 1986

Ginzburg A and Dick C E, Image information transfer properties of x-ray intensifying screens in the energy range from 17 to 320 keV *Med. Phys.*, **20**, 1013-1021, 1993

ICRU Medical Imaging - The assessment of image quality ICRU Report 54 (Bethesda, 1996)

Jennings R J, Quinn P W, Gagne R M, and Fewell T R Evaluation of x-ray source for mammography *Proc. SPIE*, **1896**, 259-268, 1993

Karlsson M, A study of some energy dependent characteristics of x-ray screens used in diagnostic radiology, Thesis, Umeå University, Sweden 1983

Lubberts G and Rossmann K, Modulation transfer function associated with geometrical unsharpness in medical radiography *Phys. Med. Biol.*, **12**, 65-77, 1967

McVey G, Dance DR, Sandborg M, Persliden J, and Alm Carlsson G, Calibration and validation of the voxel Monte Carlo code from slab phantom measurements Report RMT 97/1001, 1997.

McVey G, Dance D R, Sandborg M, Persliden J, and Alm Carlsson G, Calibration of the voxel Monte Carlo code from patient measurements Report RMT 98/1002, 1998.

Mickish D J and Beutel J, The determination of x-ray phosphor scintillation spectra *SPIE* **1231**, 327-336, 1990

Morgan R H, The frequency response function *Amer. J. Roent.*, **88**, 175-186, 1962

Nishikawa R M, Yaffe M J and Holmes R B, Effect of finite phosphor thickness on detective quantum efficiency *Med. Phys.*, **16**, 773-780, 1989

Nishikawa R M and Yaffe M J, Model of the spatial-frequency-dependent detective quantum efficiency of phosphor screens *Med. Phys.*, **17**, 894-904, 1990a

Nishikawa R M and Yaffe M J, Effect of various noise sources on the detective quantum efficiency of phosphor screens *Med. Phys.*, **17**, 887-893, 1990b

Prasad S C, Hendee W R, and Carson P L, Intensity distribution, modulation transfer function, and the effective dimension of a line-focus x-ray focal spot *Med. Phys.*, **3**, 217-223, 1976

Rao G U V, Clark R L, and Gayler B W, Radiographic magnification: a critical, theoretical and practical analysis (Part I) *Appl. Radiol.*, Jan./Feb. 37-40, 1973

Rao G U V, Clark R L, and Gayler B W, Radiographic magnification: a critical, theoretical and practical analysis (Part II) *Appl. Radiol.*, March/April 25-33, 1973

Rose A, The sensitivity of the human eye on an absolute scale *J. Opt. Soc. Am.*, **38**, 196-208, 1948

Sandborg M and Alm Carlsson G, Influence of x-ray energy spectrum, contrasting detail and detector on the signal-to-noise ratio (SNR) and detective quantum efficiency (DQE) in projection radiography *Phys. Med. Biol.*, **37** 1245-1263, 1992

Sandborg M, Dance D R, Persliden J, and Alm Carlsson G, A Monte Carlo program for the calculation of contrast, noise and absorbed dose in diagnostic radiology *Comput. Methods Prog. Biomed.*, **42**, 167-180, 1994

Sandborg M, McVey G, Dance D R, Alm Carlsson G, Persliden J, Collection and analysis of patient and image data for calibration of a voxel-phantom based Monte Carlo code and for the modelling of important structures ISRN UlI-RAD-R-085-SE, 1997

Sandborg M, Alm Carlsson G, Dance D R, Persliden J, Receptor modelling in computerised optimization of imaging systems *SPIE* Proc., **2752**, 552-563, 1996

Sandrik J M and Wagner R F, Absolute measures of physical image quality: Measurement and application to radiographic magnification *Med. Phys*, **9**, 540-549, 1982

Selwyn E W H, A Theory of graininess *Photog. J.*, **75**, 571-, 1935

Swank R K, Calculation of the modulation transfer function of x-ray fluorescent screens *Applied Optics*, **12**, 1865-1870, 1973

Tapiovaara M J, SNR and noise measurements for medical imaging: II. Application to fluoroscopic equipment *Phys. Med. Biol.*, **38**, 1761-1788, 1993

Tapiovaara M J and Sandborg M, Evaluation of image quality in fluoroscopy by measurements and Monte Carlo calculations *Phys. Med. Biol.*, **40**, 589-607, 1995

The Math Works Inc, MATLAB® The Language for technical computing 1984-1997, Version 5.1.0.The Math Works, 1997

Wagner R F and Brown D G, Unified SNR analysis of medical imaging systems *Phys. Med. Biol.*, **30**, 489-518, 1985

Ziskin M C, Revesz G, Kundel H L, and Shea F J, Spatial frequency spectra of radiographic images *Radiology*, **98**, 507-517, 1971

Zubal G I, Harrell C R, Smith E O, Ratter Z, Gindi G and Hoffer P B, Computerized three-dimensional segmented human anatomy *Med. Phys.*, **21**, 299-302, 1994